Structural variety of extended arrays of pancake-bonded TCNQ radicals: steric effect of the bulky cations

Petra Stanić,[a] Kristina Smokrović,[a] Nadica Maltar-Strmečki,[a] Mirta Herak,[b] Florian Meurer,[c,d] Michael Bodensteiner,[c] Christoph Hennig[d,e] and Krešimir Molčanov[a]*

a Ruđer Bošković Institute, Bijenička c. 54, HR-10000 Zagreb, Croatia

b Institute of Physics, Bijenička c. 46, HR-10000 Zagreb, Croatia

c Universität Regensburg, Universitätsstrasse 31, 93053 Regensburg, Germany

d Helmholtz-Zentrum Dresden-Rossendorf, Institute of Resource Ecology, Bautzner Landstraße 400, 01314 Dresden, Germany

e The Rossendorf Beamline (BM20), European Synchrotron Radiation Facility, 71 Avenue des Martyrs, 38043 Grenoble, France

KEYWORDS: TCNQ radical, pancake bonding, crystal structure, crystal engineering, magnetic measurements

ABSTRACT Six novel salts of the TCNQ radical anion with various sterically bulky cations, involving polycyclic, nonaromatic and acyclic cations were prepared and studied. The influence of sterically bulky cations on packing efficiency is studied, and it is shown that the formation of pancake bonding between TCNQ radicals is not hindered. Different arrays of stacked TCNQ, ranging from 0D (isolated radicals) to 1D (infinite chains) to 2D are described and their magnetic properties have been studied.

INTRODUCTION

Two-electron multicentre bonding (2e/mc or *pancake bonding*) is a strong intermolecular interaction which occurs between planar organic radicals [1-4]. It involves the pairing of spins of contiguous radicals due to the extending of the highest occupied molecular orbital (HOMO) between both rings; this implies a significant covalent contribution to the total interaction, which often exceeds −15 kcal mol^{-1} [1]. Other significant components of interaction are electrostatic, dispersion and attraction of (local) dipoles. Therefore, pancake bonding is one of the strongest intermolecular interactions, comparable to the strong hydrogen [5,6] and halogen bonds [7,8], which are also partially covalent. However, in pancake bonding, the electron pair is not localized, but distributed between two radicals, involving multiple centers [1-4]. Bulk properties of radical-based materials are defined by degree of pancake bonding [3,4], so it is interesting not only from the fundamental aspects as nature of chemical bonding and intermolecular interactions, but also from applicative point of view. Fine-tuning of this interaction may lead to the design of novel organic magnets and (semi)conductors [9-16].

Discrete (0D) motives of pancake-bonded dimers or trimers typically result in diamagnetic or antiferromagnetic properties of bulk samples [3,4] and are therefore of less interest. These oligomers often stack by weaker (non-bonding) interactions.

Extended 1D motives are characterized by (nearly) equidistant radicals with an interplanar separation shorter than 3.2 Å. The close contacts allow electron jumps between the rings and long-range magnetic ordering; therefore, the bulk materials are mostly semiconductive and antiferromagnetic [3,4]. Stacks of ionic radicals are weaker conductors with conductivities mostly below 10^{-6} S cm^{-1} [17-21], while neutral radicals are better conductors by 4 - 5 orders of magnitude [11,12,14,15,20-26]. However, these crystals are conductive only in the direction of stacking.

Pancake bonding extending in 2D arrays was observed in salts of 7,7,8,8-tetracyanoquinodimethane radical anion (TCNQ, Scheme 1) [27]. It involves spin interactions and electron transport in two directions (as evidenced by electron paramagnetic resonance (EPR) spectroscopy) and conductivity up to 10^{-2} S cm^{-1} has been reported [27]. Therefore, such 2D pancake-bonded systems may be more interesting than 1D stacks, however, there are only a few germinal studies. It is known that TCNQ readily reacts with electron donors forming salts of various stoichiometries; its formal charge is often partial, −1/2 or −2/3. There are also many unknowns which may influence the stacking of TCNQ: aromaticity and steric influence of the cation, competition with other strong intermolecular interactions (hydrogen and halogen bonding), formation of mixed stacks with electron donors or cations, etc. However, almost all organic TCNQ salts comprise aromatic rings, and are mostly planar. A systematic study of salts of TCNQ with non-aromatic and acyclic cations would therefore be of high interest.

To provide at least a partial answer, in this work, we present six novel salts of partially charged TCNQ radical anion with different sterically bulky cations, involving polycyclic planar aromatic

[tetrazolium and *N*-(4-iodobenzyl)-2-iodopyridinium], polycyclic non-planar aromatic (1,1'-methylenedipyridinium), non-planar non-aromatic (dabco) and acyclic (*N*,*N*,*N*,*N*',*N*',*N*'-hexamethyl-1,2-ethanediaminium).

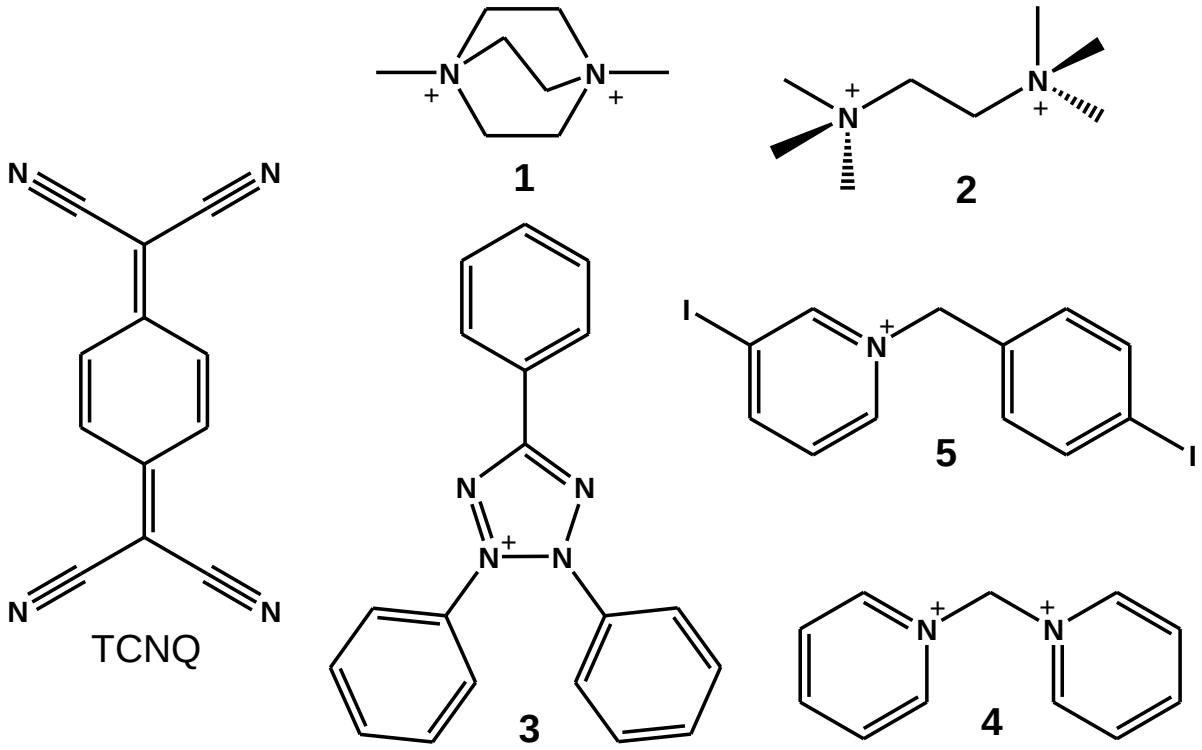

Scheme 1 TCNQ radical anion and cations used in this work: 1,4-dimethyl-1,4-diazabicyclo[2.2.2]octanium (dabco, **1**), *N*,*N*,*N*,*N*',*N*',*N*'-hexamethyl-1,2-ethanediaminium (**2**), tetrazolium (**3**), 1,1'-methylenedipyridinium (**4**) and *N*-(4-iodobenzyl)-3-iodopyridinium (**5**).

RESULTS AND DISCUSSION

Crystal packing and pancake bonding in the novel TCNQ salts

The following compounds were prepared and characterised: **1**·I·TCNQ, $\mathbf{1}_2$·$TCNQ_5$·MeCN, **2**·$TCNQ_2$·MeCN, $\mathbf{3}_2$·$TCNQ_3$, **4**·$TCNQ_3$ and **5**·$TCNQ_2$.

The asymmetric unit of **1**·I·TCNQ comprises a half of a C_2-symmetric cation of **1** (the twofold axis passes through the center of C15-C15' bond), a half of an iodide anion (also located on a twofold axis) and a half of a centrosymmetric TCNQ moiety. In **2**·$TCNQ_2$·MeCN a TCNQ moiety is located on a mirror plane (therefore p.p. is 0.5) and a cation of **2** is located in a special position with a molecular symmetry of C_{2v} (a quarter of a cation is symmetry-independent); in addition, there is a half of an acetonitrile molecule disordered about an inversion center. In $\mathbf{3}_2$·$TCNQ_3$ there are two symmetry-independent tetrazolium cations and four TCNQ moieties, two of which have a C_1 symmetry (A and B) and the other two are centrosymmetric (C and D; therefore, a half of each moiety is in asymmetric unit). The asymmetric unit of **4**·$TCNQ_3$ comprises a half of a mirror-symmetric cation (its central methylene C is located in a mirror plane), one TCNQ moiety in a general position and another TCNQ moiety located in a mirror plane (therefore p.p. is 0.5). Asymmetric unit in **5**·$TCNQ_2$ comprises one cation of **5** and two TCNQ moieties; in $\mathbf{1}_2$·$TCNQ_5$·MeCN there are two symmetry-independent cations of **1**, five TCNQ moieties and one molecule of acetonitrile.

The formal charges of TCNQ moieties are −1/2 in **1**·I·TCNQ, **2**·$TCNQ_2$·MeCN and **5**·$TCNQ_2$, −2/3 in $\mathbf{3}_2$·$TCNQ_3$ and **4**·$TCNQ_3$ and −4/5 in $\mathbf{1}_2$·$TCNQ_5$·MeCN. However, the correlation of molecular geometry [28] indicates that four TCNQ moieties in $\mathbf{1}_2$·$TCNQ_5$·MeCN (labelled as A, B, D and E) have a full negative charge (i.e. −1), while the moiety C is neutral or very close to neutral (Tables S1 and S2). Since it is known that pancake bonding and molecular environment (i.e. crystal field) cause a distortion of the molecule comparable to geometry changes caused by charge [27,29], the estimation of charge from geometric correlations is unreliable [30] and should be used with caution, even for high-quality structures with low *R* and small standard deviations of

bond lengths. A more accurate assessment can be obtained by quantum chemical computations or X-ray charge density measurements [31].

Among the studied systems, crystal packing of **1**·I·TCNQ is unique, as it involves essentially isolated TCNQ radicals with very weak stacking interactions unfavourable for pancake bonding interactions (Table 1, Fig. 1a). Despite interplanar separation of 3.225 Å, the closest contact between TCNQ moieties involves an extremely large offset of 6.973 Å; thus, overlap between the contiguous TCNQ moieties is negligible. Another unique feature of **1**·I·TCNQ is the presence of iodide anions (making it the first TCNQ salt co-crystallised with iodide), which occupy interstices in the lattice comprised of cations and TCNQ moieties (Fig. 1b). There are two symmetry-independent weak hydrogen bonds linking the cations and TCNQ (Table 2), but no directed interactions with the iodide anions.

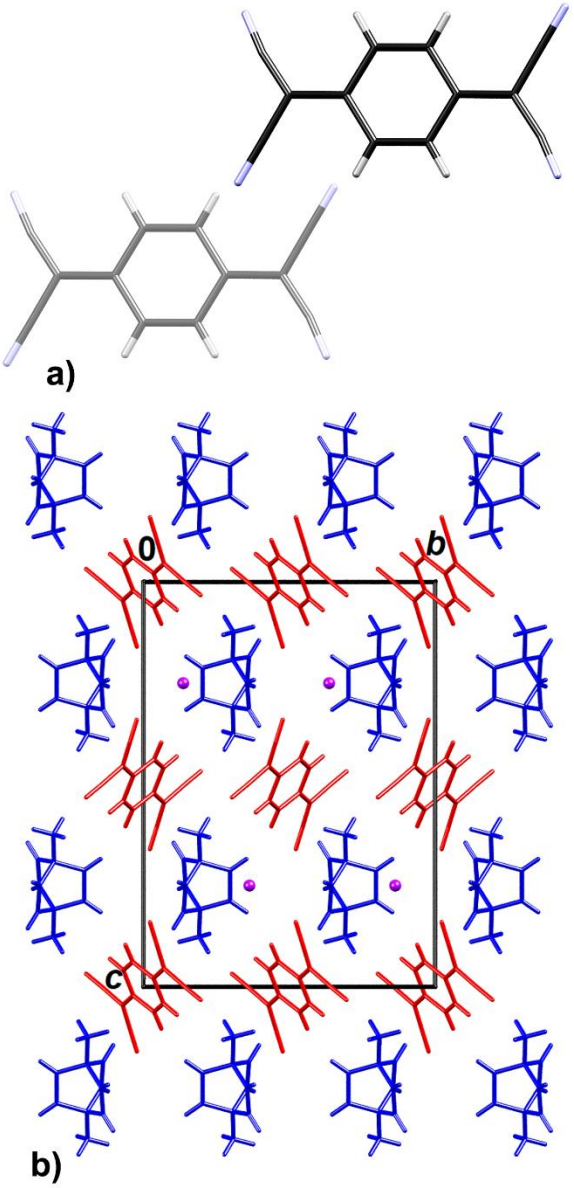

Figure 1 a) a pair of TCNQ radicals (related by symm. op. 3/2−*x*, −1/2+*y*, 1/2−*z*) in **1**·I·TCNQ viewed normal to the ring planes. The bottom radical is shown in a pale colour. b) Crystal packing viewed in the direction [100]. TCNQ moieties are shown red, cations of **1** are blue and iodide anions are shown as purple spheres of arbitrary radii.

Table 1 Geometric parameters of π interactions.

π···π	Cg[a]···Cg / Å	α[b]	β[c]	δ[d]	ε[e]	Cg···plane(Cg2) / Å	Offset/ Å[f]	Symm. op. on Cg2
1·I·TCNQ								
C3→C11···C3→C11	7.897(4)	0.0	62.0	0.0	35.6	3.225(3)	6.973	3/2−x, −1/2+y, 1/2−z
C3→C11···C3→C11	8.119(4)	0.0	63.0	0.0	3.3	3.721(2)	7.234	1−x, −y, −z
1$_2$·TCNQ$_5$·MeCN								
C3A→C11A···C3B→C11B	3.3028(12)	1.68(9)	13.9	3.0	85.8	3.2210(8)	0.793	1+x, y, z
C3C→C11C···C3D→C11D	4.0815(12)	3.36(9)	36.2	63.4	75.1	3.4195(9)	2.411	x, y, z
C3D→C11D···C3E→C11E	3.2746(11)	2.80(9)	16.0	3.2	90.0	3.1798(8)	0.905	x, y, z
C3A→C11A···C3C→C11C	4.8189(13)	3.39(10)	46.0	59.9	87.2	3.3362(8)	3.467	1+x, y, z
C3A→C11A···C3C→C11C	5.4005(13)	3.39(10)	53.4	61.8	87.2	3.2217(8)	4.337	2+x, y, z
C3B→C11B···C3E→C11E	4.8833(12)	0.74(9)	46.0	1.1	32.8	3.3719(8)	3.511	x, y, 1+z
2·TCNQ$_2$·MeCN								
C3→C11···C3→C11	3.8676(11)	0.0	33.3	0.0	0.0	3.2323	2.124	1/2−x, 1/2+y, 3/2−z
3$_2$·TCNQ$_3$								

C3A→C11A···C3A→C11A	3.951(2)	0.00(16)	31.0	0.0	5.4	3.3883(14)	2.032	2−x, −y, −z
C3A→C11A···C3C→C11C	3.785(2)	1.02(16)	32.3	3.4	3.5	3.1833(14)	2.020	x, y, z
C3B→C11B···C3B→C11B	3.8033(16)	0.00(13)	34.2	0.0	0.5	3.1465(11)	2.136	1−x, 1−y, −z
C3B→C11B···C3D→C11D	3.8583(17)	1.00(14)	31.3	2.1	1.7	3.3091(11)	2.004	x, y, z
4·$TCNQ_3$								
C3A→C11A···C3A→C11A	5.0492(13)	1.19(11)	50.1	1.2	59.5	3.2511(9)	3.873	−1/2+x, 1/2−y, z
C3A→C11A···C3B→C11B	3.7783(13)	0.59(7)	33.3	8.2	1.0	3.1504(1)	2.072	x, y, z
5·$TCNQ_2$								
C3A→C11A···C3A→C11A	3.848(2)	0.00(18)	28.1	0.0	0.0	3.3962(16)	1.811	−x, 1−y, −z
C3A→C11A···C3A→C11A	3.840(2)	0.00(18)	32.4	0.0	0.0	3.2420(16)	2.057	1−x, 1−x, −z
C3B→C11B···C3B→C11B	3.890(2)	0.00(19)	32.4	0.0	7.4	3.2841(16)	2.085	1−x, 2−y, −z
C3B→C11B···C3B→C11B	4.004(2)	0.00(19)	32.7	0.0	7.4	3.3677(16)	2.166	2−x, 2−y, −z
C19→C24···C19→C24	4.073(2)	0.0(2)	35.1	-	-	3.3302(18)	2.345	2−x, 1−y, 1−z

[a] Cg = centre of gravity of the aromatic ring.

[b] α = angle between planes of two interacting rings.

[c] β = angle between Cg···Cg line and normal to the plane of the first interacting ring.

[d] δ = torsion angle between molecular axes C=C...C=C, described in ref. [53].

[e] ε = direction of offset, described in ref. [53].

f

1D arrangement of TCNQ moieties (infinite stacks) are present in **2**·$TCNQ_2$·MeCN and $\mathbf{3}_2$·$TCNQ_3$. In the former, the radicals are equidistant (Table 1, Figure 2a) with an interplanar separation of 3.232 Å. Three symmetry-independent C−H···N hydrogen bonds link the *N*,*N*,*N*,*N*',*N*',*N*'-hexamethyl-1,2-ethanediaminium and TCNQ radicals (Table 2); the packing achieved is thus porous, with large channels occupied by disordered solvent acetonitrile molecules (Fig. 2b).

A new stacking motive is observed in $\mathbf{3}_2$·$TCNQ_3$, which involves two longer and one shorter interplanar separations (Table 1). There are two symmetry-independent stacks extending in the [010] direction, one comprising TCNQ moieties A and C stacked in the sequence ...AACAA...; the other stack involves moieties B and D stacked in the sequence ...BBDBB... (Fig. 3a). Stacks with the same sequence have been observed in other salts of TCNQ [27] and some semiquinones [29,31]; in all of them the formal charge of the radical is −2/3. The stacks ...AACAA... and all previously described stacks [29,31] involve pancake-bonded trimers characterised by two short and one long distances, while stacks ...BBDBB.... involve one shorter and two longer distances. Rings C and D are centrosymmetric, while A and B have a molecular symmetry of C_1. Therefore, the stacks ...BBDBB.... can be described as 'inverse trimers' BDB. For the highly accurate structure

determined at 100 K, geometric correlation [28] gave reasonable charges: for a trimer ACA it is −1.87, and for an 'inverse' trimer BDB it is −1.85, close to formal values of −2. In an 'inverse' BDB the lateral rings B have a higher negative charge than the central ring D (−0.85 and −0.19, respectively) and in the trimer ACA, the central ring C has higher charge of −0.85, while the lateral rings A have charge of −0.51 (Tables S1 and S2), similar to other previously described trimers [29,31]. Large tetrazolium cations act as barriers between individual stacks of cations preventing the formation of 2D array (Fig. 3b).

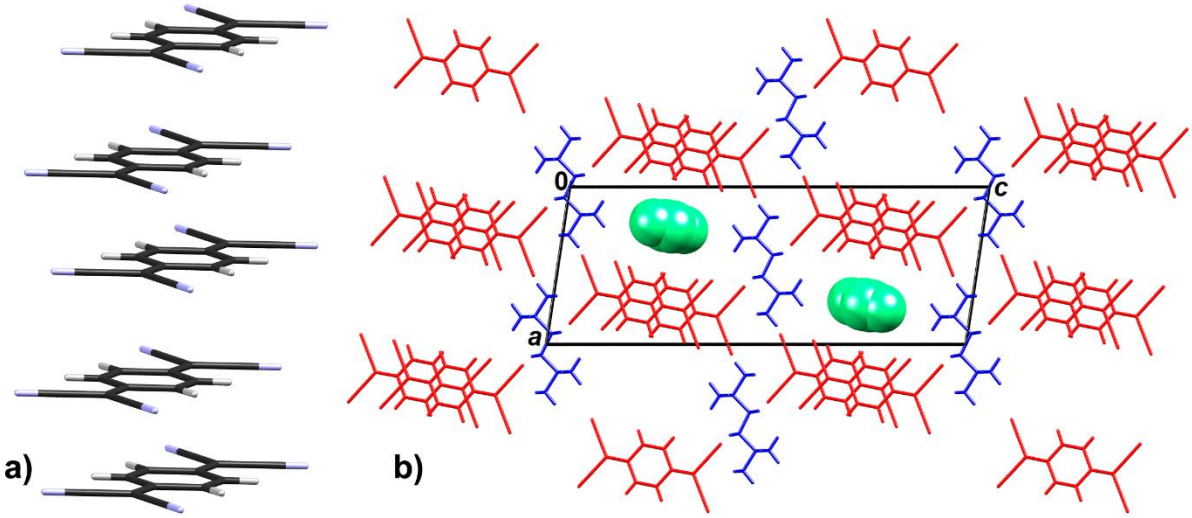

Figure 2 a) A stack of equidistant radicals in **2**·$TCNQ_2$·MeCN. b) Crystal packing viewed in the direction [010]. TCNQ moieties are shown red, cations of **2** are blue and disordered acetonitrile molecules are shown as green van der Waals spheres.

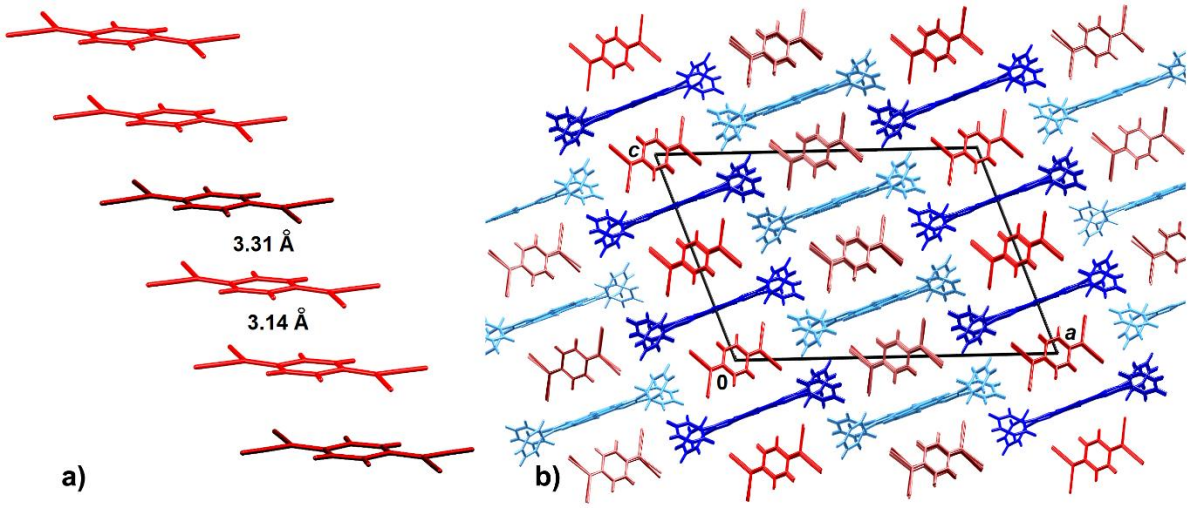

Figure 3 a) The 'inverse trimers' in a stack of TCNQ radicals in $\mathbf{3}_2$·$TCNQ_3$. Long and short interplanar separations are marked. b) crystal packing of $\mathbf{3}_2$·$TCNQ_3$ viewed in the direction [101]. Symmetry-independent moieties of TCNQ are shown as different shades of red, and cations of **3** as light and dark blue.

Stacks of 'regular' trimers [27,29,31] are present in **4**·$TCNQ_3$, and are arranged in a 2D 'brick-wall' pattern (Table 1, Fig. 4a). The direction of stacking is [010], and the layers are parallel to the (001) plane. The radical trimers are similar to those previously described in a salt of tetrachlorosemiquinone and 4-dimethylamino-*N*-methylpyridinium [31], where the semiquinone trimer has a total charge of −2. The central ring B is centrosymmetric, while two lateral rings A have a molecular symmetry *Ci*. According to geometry, the central ring B has a more negative charge (−0.75) than lateral rings A (−0.50); the total charge of a trimer is then −1.75 (Tables S1 and S2), reasonably close to the formal value of −2 and similar to values in a trimer of tetrachlorosemiquinone radical anions obtained from charge density studies [31]. Neighbouring stacks are connected by C−H···N hydrogen bonds (Table 2). Distances between the trimers are

relatively short (3.25 Å), indicating long-range interactions. The crystal packing is layered, with alternating layers of TCNQ and cations (Fig. 4b).

Stacks of pancake-bonded dimers, connected through C−H···N hydrogen bonds into a 2D 'brick-wall' network (Tables 1 and 2, Fig. 5a) are the main feature of the crystal packing of **5**·$TCNQ_2$. Two symmetry-independent radicals A and B form separate symmetry-independent stacks (Fig. 5a) extending in the [100] direction. Weak stacking interactions are also observed between **5** cations (Table 1), which are connected to each other through halogen bonding (Table 3). The crystal packing is layered, with alternating layers of anions and cations (Fig. 5b).

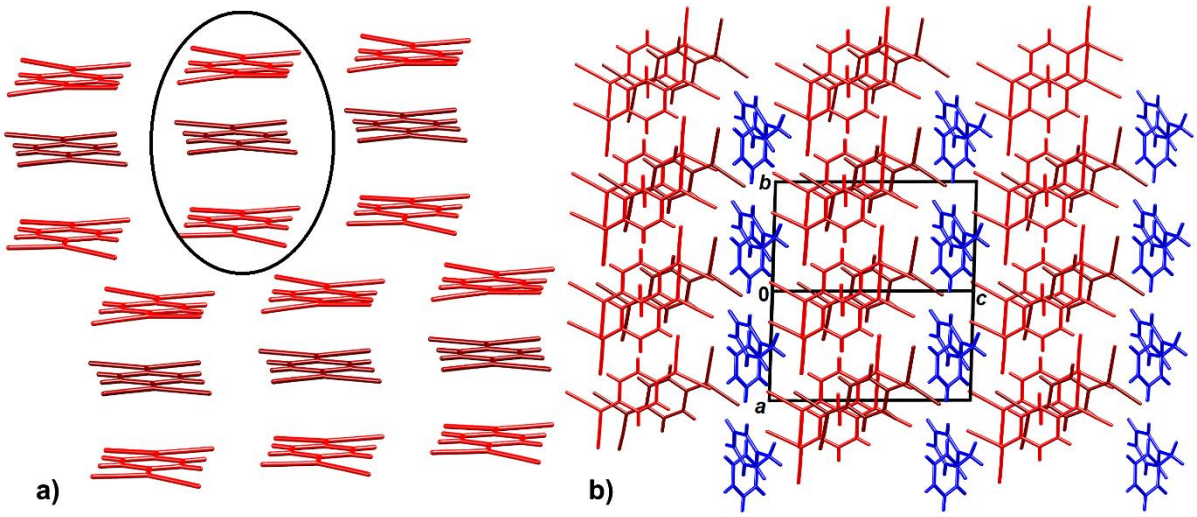

Figure 4 a) a 'brick-wall' layer of 'inverse trimers' of TCNQ radicals in **4**·$TCNQ_3$ and b) crystal packing viewed in the direction [110]. TCNQ moiety A is red, B is dark red and cations of **4** are blue. A trimer is highlighted.

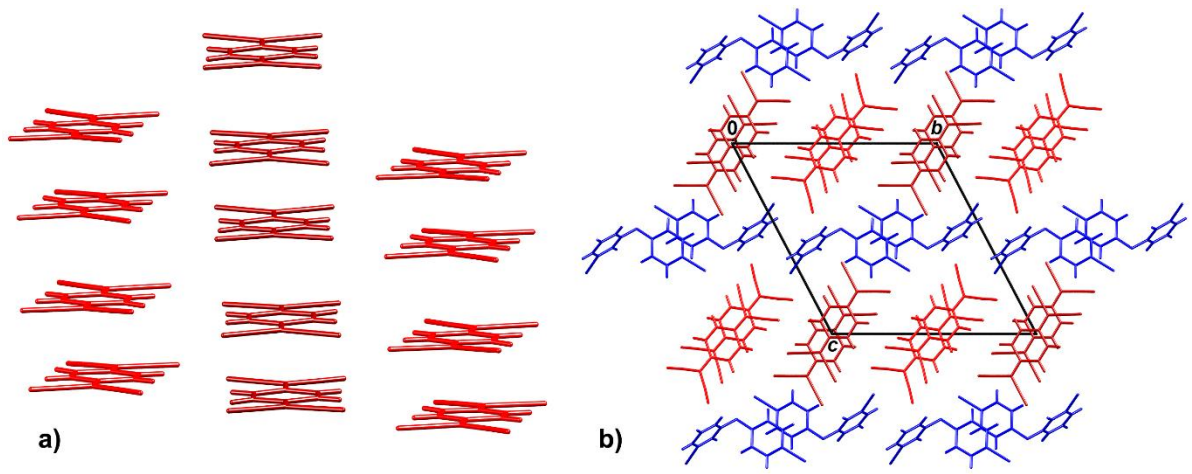

Figure 5 a) a 'brick-wall' layer of pancake-bonded dimers of TCNQ radicals in **5**·$TCNQ_2$ and b) crystal packing viewed in the direction [100]. TCNQ moiety A is red, B is dark red and cations of **5** are blue.

The crystal packing of $\mathbf{1}_2$·$TCNQ_5$·MeCN is unprecedented, with a five symmetry-independent TCNQ moieties (labelled as A, B, C, D, E) and two **1** cations (A and B). Four radicals stack in the sequence ABED (Fig. 6a) in the direction [001]. Contacts A-B and D-E correspond to pancake bonding, while contact B-E is longer and can be regarded as an inter-dimer nonbonding contact (Table 1). Neutral TMPD moieties C form hydrogen-bonded chains parallel to [100] and are embedded between the tetramers ABED (Fig. 6a). Their molecular axes C=C...C=C are not parallel to the other radicals, but inclined by some 60º; they form weaker stacking contacts with radicals A and D (Table 1). These layers of TCNQ radicals are parallel to (010); between them are layers of cations and solvent acetonitrile molecules (Fig. 6b). The entire structure is held together by an extensive network of C−H···N hydrogen bonds (Table 2).

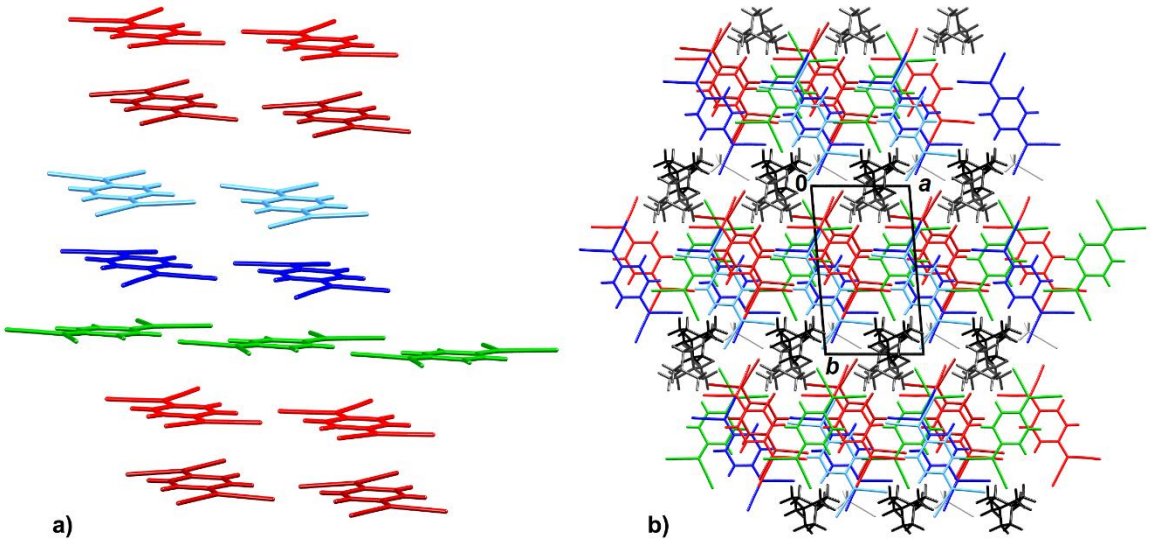

Figure 6 a) a 2D layer of TCNQ moieties parallel to (010) in **1**$_2$·TCNQ$_5$·MeCN and b) crystal packing viewed in the direction [001]. TCNQ moiety A is light red, B is dark red, C is green, D is dark blue and E is light blue; cations of **1** are black and acetonitrile molecules are red.

Table 2 Geometric parameters of hydrogen bonds (Å, °).

	D–H / Å	H···*A* / Å	*D*···*A* / Å	*D*–H···*A* / º	Symm. op. on *A*
1·I·TCNQ					
C15–H15···N3	0.93	2.41	3.229(19)	148	−1/2+*x*, 1/2−*y*, −1/2+*z*
C19–H19B···N1	0.96	2.49	3.384(15)	155	3/2−*x*, −1/2+*y*, 1/2−*z*
1$_2$·TCNQ$_5$·MeCN					
C13B–H13C···N4D	0.97	2.56	3.498(4)	162	*x*, *y*, 1+*z*
C13B–H13D···N7	0.97	2.60	3.458(6)	148	*x*, −1+*y*, *z*
C14A–H14A···N2A	0.97	2.54	3.407(3)	150	−1+*x*, 1+*y*, *z*
C14B–H14C···N2D	0.97	2.60	2.994(4)	105	*x*, *y*, *z*
C15A–H15B···N3A	0.97	2.55	2.982(4)	107	*x*, *y*, *z*

C16B–H16D···N3E	0.97	2.47	3.324(4)	147	1+*x*, −1+*y*, *z*
C17A–H17A···N2B	0.97	2.41	3.293(4)	151	*x*, 1+*y*, *z*
C17B–H17D···N3D	0.97	2.56	3.454(3)	153	1+*x*, −1+*y*, *z*
C19B–H19E···N7	0.96	2.57	3.429(5)	150	*x*, −1+*y*, *z*
C20A–H20A···N2A	0.63	2.62	3.475(4)	149	−1+*x*, 1+*y*, *z*
C22–H22C···N3A	0.98(3)	2.62(4)	3.355(4)	132(3)	−1+*x*, *y*, *z*
2·$TCNQ_2$·MeCN					
C13–H13A···N3	0.97	2.59	3.505(2)	158	1/2−*x*, 1/2+*y*, 3/2−*z*
C13–H13B···N3	0.97	2.59	3.505(2)	158	1/2−*x*, −1/2+*y*, 3/2−*z*
C15–H15C···N4	0.96	2.60	3.471(8)	151	−*x*, *y*, 1−*z*
$\mathbf{3}_2$·$TCNQ_3$ **100K**					
C16A–H16A···N2B	0.93	2.71	3.371(5)	129	1−*x*, 1−*y*, −*z*
C18A–H18A···N4A	0.93	2.46	3.291(4)	149	*x*, 3/2−*y*, 1/2+*z*
C24A–H24A···N2A	0.93	2.49	3.271(4)	142	*x*, *y*, *z*
C30A–H30A···N8A	0.93	2.72	3.625(4)	166	2−*x*, 1/2+*y*, 1/2−*z*
C15B–H15B···N4A	0.93	2.74	3.497(5)	139	1−*x*, 1−*y*, −*z*
C16B–H16B···N1A	0.93	2.75	3.537(4)	143	−1+*x*, 1+*y*, *z*
C18B–H18B···N2B	0.93	2.48	3.312(4)	149	*x*, 1+*y*, *z*
C21B–H21B···N1C	0.93	2.71	3.401(4)	132	1−*x*, 1−*y*, −*z*
C24B–H24B···N3D	0.93	2.50	3.309(4)	146	*x*, 1/2−*y*, 1/2+*z*
C30B–H30B···N8B	0.93	2.48	3.312(4)	166	1−*x*, 1/2+*y*, 1/2−*z*
4·$TCNQ_3$					
C5A–H5A···N4A	0.93	2.60	3.289(4)	131	1+*x*, *y*, *z*
C10A–H10A···N1B	0.93	2.62	3.304(4)	131	−1+*x*, *y*, *z*
C14–H14···N3B	0.93	2.55	3.434(6)	158	*x*, *y*, 1+*z*
C15–H15···N3A	0.93	2.47	3.231(6)	139	*x*, 1−*y*, 1+*z*

C16–H16···N2A	0.93	2.50	3.390(6)	159	−1/2+*x*, 1/2+*y*, *z*
C17–H17···N2A	0.93	2.47	3.344(7)	156	−1+*x*, 1−*y*, *z*
C18–H18···N2B	0.93	2.50	3.388(6)	160	−1+*x*, *y*, *z*
5·$TCNQ_2$					
C4B–H4B···N4A	0.93	2.59	3.202(7)	123	1+*x*, *y*, *z*
C13–H13···N2B	0.93	2.51	3.343(7)	149	1−*x*, 2−*y*, −*z*
C20–H20···N3B	0.93	2.36	3.226(6)	154	*x*, *y*, *z*

Table 3 Short halogen...halogen distances.

	d / Å	C–Br···I / º	symm. op. on Br
5·$TCNQ_3$			
C22-I2···N3A	3.348(5)	153.50(14)	1+*x*, *y*, *z*
C14-I1···N4A	3.683(7)	149.35(18)	−*x*, 2−*y*, −*z*

Magnetic properties of the studied compounds

The EPR spectra were recorded at room temperature (RT) and the corresponding simulations for five investigated complexes studied (**1**·I·TCNQ, $\mathbf{1}_2$·$TCNQ_5$·MeCN, **2**·$TCNQ_2$·MeCN, $\mathbf{3}_2$·$TCNQ_3$ and **5**·$TCNQ_2$) are shown in Figure 7. **1**·I·TCNQ, **2**·$TCNQ_2$·MeCN and **5**·$TCNQ_2$ consist of a single line with an effective *g*-value in the range of 2.0033–2.0040, indicating the presence of an organic radical and consistent with previous results [32]. $\mathbf{1}_2$·$TCNQ_5$·MeCN and $\mathbf{3}_2$·$TCNQ_3$ have more complex spectral composition, but the effective *g*-value is in the same range (Table 4). The results shown are for the simulations using a two-component system, i.e. there are two magnetically non-equivalent species present.

For further analysis, the EPR intensity, I_{EPR}, the peak-to-peak intensity, I_{pp} peak-to-peak linewidth, effective *g*-value and A/B, as measure of asymmetry of EPR lines (as explained in Fig. S13), have been examined as a function of temperature (Fig. S14-S18). The EPR intensity, I_{EPR}, is defined as the integral under the absorption line (area under the curve). In addition, spin susceptibility, χ_{spin} has been determined as a measure of the imaginary part of the dynamic susceptibility and consequently measure of the local spin susceptibility, in contrast to the other magnetization methods, which measure the total susceptibility of the sample (χ).

Figure 8 shows that the intensities of the lines do not follow Curie's law and exhibit a complex dependence. At RT, the asymmetry parameters A/B do not indicate conductivity, but temperature dependences (Fig. S21) show temperature dependent EPR line width asymmetry. Complex behavior is confirmed also with temperature dependence of EPR spin susceptibility (Figure 9), g_{eff} (Fig. S19) and EPR linewidth (Fig. S20). To get insight in the mechanisms behind these observations, further single crystal measurements of samples are in progress.

Complex EPR spin susceptibility temperature behavior for **2**·$TCNQ_2$·MeCN sample is further confirmed by magnetization study, as will be shown below.

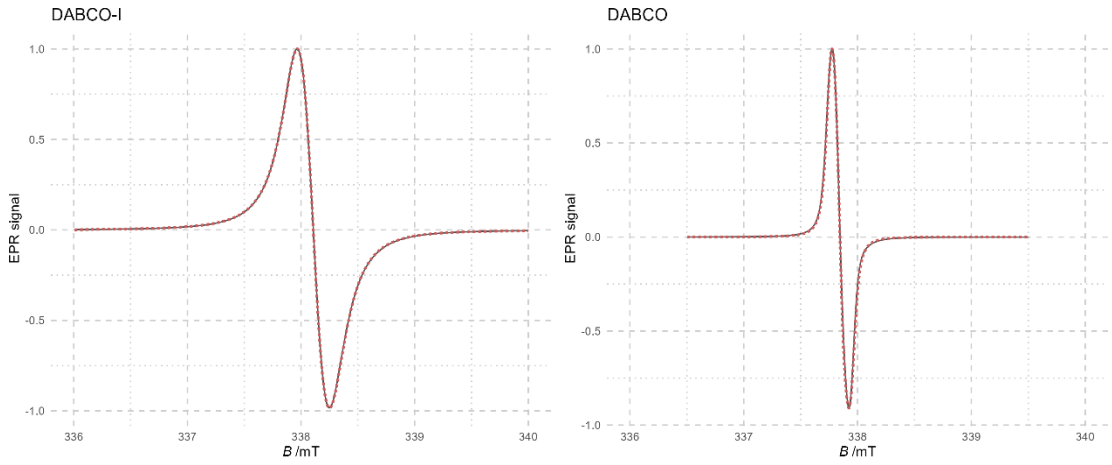

a) **b)**

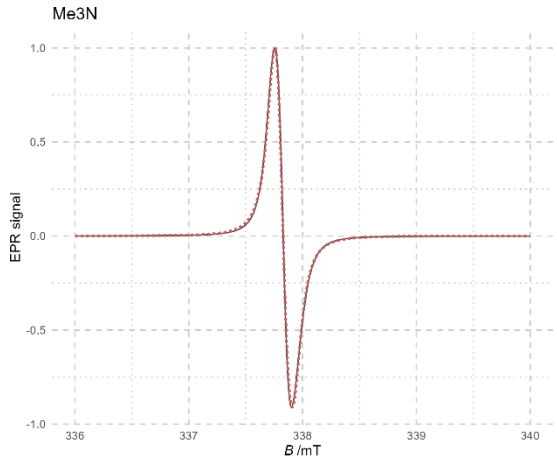

c)

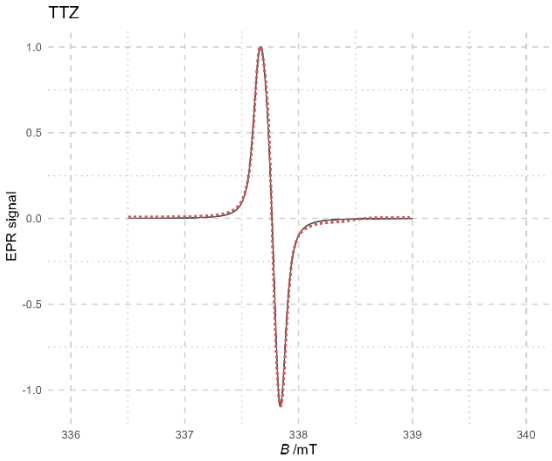

d)

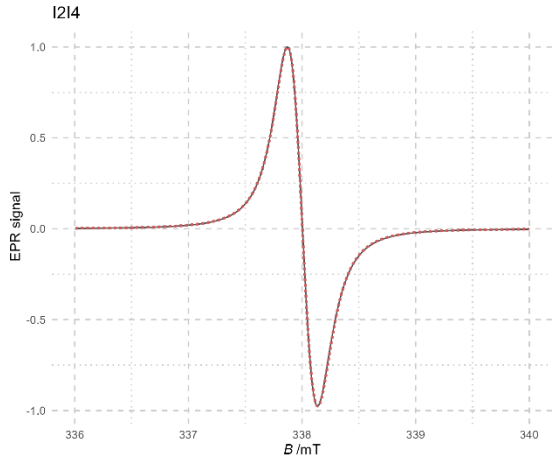

e)

Figure 7 EPR spectra at room temperature for samples a) **1**·I·TCNQ, b) **1**$_2$·TCNQ$_5$·MeCN, c) **2**·TCNQ$_2$·MeCN, d) **3**$_2$·TCNQ$_3$ and e) **5**·TCNQ$_2$ (solid black line experimentally detected, dashed red line simulation).

Table 4 EPR data extracted for simulation of experimental spectra obtained at RT.

Sample	*g*	g_{eff}	Lorenz/mT	Gauss/mT	A/B	weight

2·$TCNQ_2$·MeCN	2.00400 2.00397 2.00331	2.00376	0.0982	0.0524	1.0993	1
5·$TCNQ_2$	2.00418 2.00422 2.00337	2.00392	0. 2021	0.0950	1.0255	1
1·I·TCNQ	2.00376 2.00376 2.00296	2.00350	0. 2146	0.1113	1.0172	1
$\mathbf{1}_2$·$TCNQ_5$·MeCN	2.00417 2.00401 2 .00345 2 .00135 2 .00272 2 .00353	2.00388	0 .0201 0 .4202	0 .1042 0 .5491	1.1005	0 .9106 0.0894
$\mathbf{3}_2$·$TCNQ_3$	2.00303 2.00408 2.00422 2.00331 2.00367 2.00454	2.00375	0.0801 0.0183	0.0268 0.0592	0.9141	0.9630 0.0370

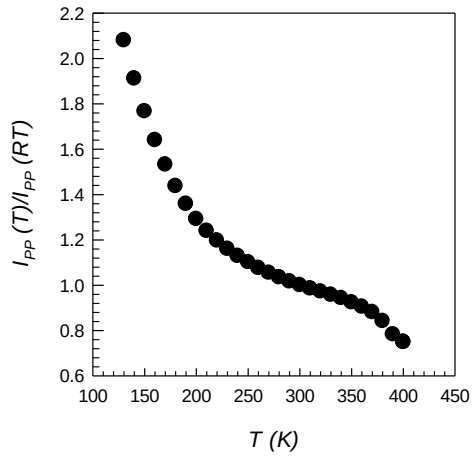
I_{PP} (T)/I_{PP} (RT)
T (K)

a)

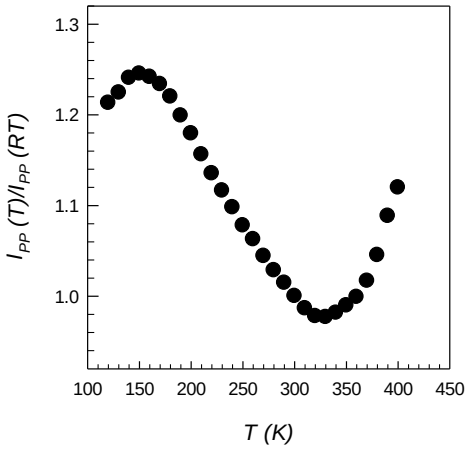
I_{PP} (T)/I_{PP} (RT)
T (K)

b)

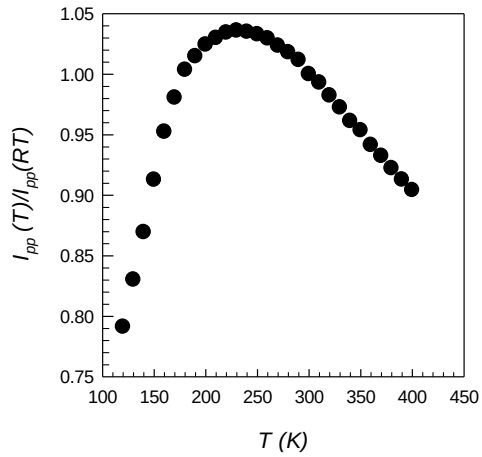
I_{pp} (T)/I_{pp}(RT)
T (K)

c)

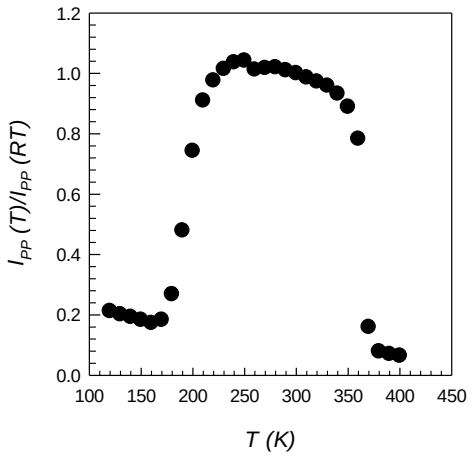
I_{PP} (T)/I_{PP} (RT)
T (K)

d)

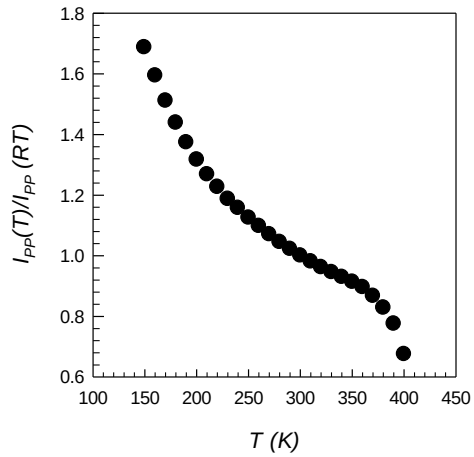
I_{Pp}(T)/I_{PP} (RT)
T (K)

e)

Figure 8 Temperature dependence of peak-to peak EPR intensity spectra $I_{EPR}(T)$, normalized with respect to room temperature value $I_{EPR}(RT)$ for samples a) **1**·I·TCNQ, b) $\mathbf{1}_2$·$TCNQ_5$·MeCN, c) **2**·$TCNQ_2$·MeCN, d) $\mathbf{3}_2$·$TCNQ_3$ and e) **5**·$TCNQ_2$

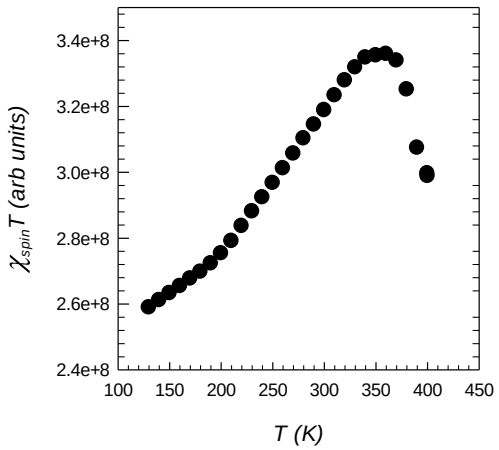

a)

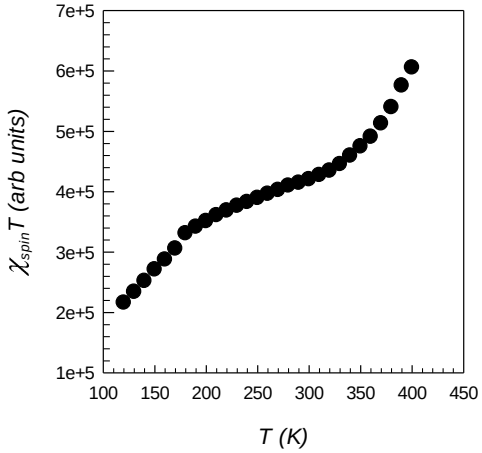

b)

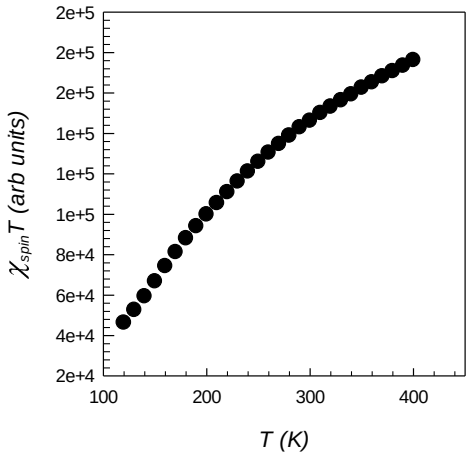

c)

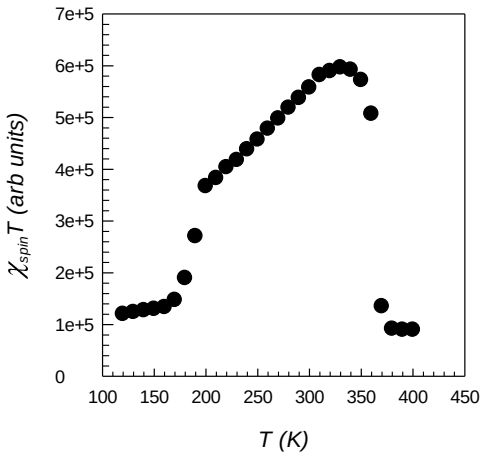

d)

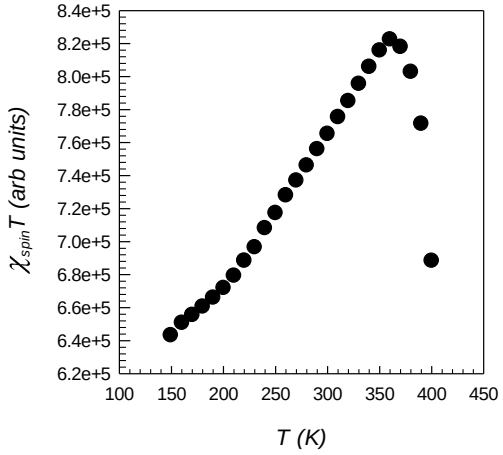

e)

Figure 9 spin susceptibility vs. temperature for samples a) **1**·I·TCNQ, b) $\mathbf{1}_2$·$TCNQ_5$·MeCN, c) **2**·$TCNQ_2$·MeCN, d) $\mathbf{3}_2$·$TCNQ_3$ and e) **5**·$TCNQ_2$.

In Fig. 10 temperature dependence of magnetic susceptibility measured from 5 K to 400 K is shown for each of the five samples. The separately measured diamagnetic contribution of the sample holder has been subtracted from the data. We see that the total susceptibility is positive only for samples **1**·I·TCNQ and **2**·$TCNQ_2$·MeCN, while the other three samples display negative susceptibility in most of the temperature range. Subtracting the expected diamagnetic contribution [33] still leaves the susceptibility negative for these samples (Fig. S22). In Fig. 10 we also plot the curves representing the Curie law which would be obtained if the electron spins on TCNQ moieties were noninteracting. The number of electrons per formula unit was obtained by taking into account the formal charge of TCNQ moieties. For **1**·I·TCNQ and **2**·$TCNQ_2$·MeCN, which have positive susceptibilities, this demonstrates that the interactions between the spins formed on stacked motifs of TCNQ moieties are very strong and antiferromagnetic since the measured susceptibilities have much smaller magnitudes than what would be obtained from Curie law representing the

noninteracting spins. For **1**·I·TCNQ and **2**·$TCNQ_2$·MeCN this is also visible in the $\chi(T) \cdot T$ plot given in insets of Fig. 10a and 10c, respectively, where we see that $\chi(T) \cdot T$ does not saturate at high temperatures, as would be expected if magnetic interactions were weak. This result is corroborated by the results obtained by EPR, which probes the spin only susceptibility, shown in Fig. 9a and 9c. The differences in the temperature dependencies of the EPR and dc susceptibility results are due to the fact that EPR probes spin-only contributions, while dc susceptibility is sensitive to all magnetic contributions. The small "bumps" in susceptibility observed around 50-60 K for some samples most likely represent the oxygen peak which is often observed for powder samples with small signal when small amounts of air and oxygen are trapped inside the capsule and between the grains of powder.

Taking into account the reported crystal structure and charge distribution, we can attempt to interpret the obtained data for **2**·$TCNQ_2$·MeCN. The magnetic lattice is expected to be formed by TCNQ moieties stacked in a zig-zag fashion along the *b* axis with one spin per two TCNQs (1 spin $S = 1/2$ per f.u.). We, therefore, assume that the magnetic response of this system can be described as the $S = 1/2$ 1D Heisenberg antiferromagnet with the contribution of a small amount of the $S = 1/2$ impurities. We fit the susceptibility to the following expression:

$$\chi_{\text{spin}}(T) = c_i \chi_{\text{imp}}(T) + (1 - c_i) \chi_{\text{1D HAF}}(J,T) + \chi_0 \quad (1)$$

where the first term describes the contribution of c_i impurities per mole, the second term is the susceptibility of the Heisenberg $S = 1/2$ 1D antiferromagnet [34] and the third term is temperature-independent diamagnetic contribution. Since magnetization measured in 3 T is not strictly linear in the magnetic field at the lowest temperatures, we do not use Curie-Weiss law for $\chi_{\text{imp}}(T)$ but rather magnetization described by Brillouin function divided by magnetic field. We assume that the impurities come from the same surrounding as the main contribution, possibly from the

structurally distorted chains, which is corroborated by the fact that a single EPR line is observed in the EPR spectra of this system. The results obtained from the fit are c_i = 0.04912(2), J/k_B = 507(2) K and $\chi_0 = -1.96(2)\cdot10^{-4}$ emu/mol. In Fig. 11 we plot curve (1) with parameters obtained from the fit. We see that the agreement between the data and the fitted curve is very good. Good agreement is obtained also with *M* vs *H* curves measured at several low temperatures (Fig. S23).

Large AFM 1D interaction was also reported previously for a charge-transfer system of TCNQ with tetrathiafulvalene (TTF·TCNQ) [35]. The low-*T* upturn can occur in systems with antisymmetric Dzyaloshinskii-Moriya interaction (DMI) [36,37] where it can mimic the behaviour displayed by impurities [38-41]. However, the inversion center placed between the molecules does not allow the presence of DMI. The 1D HAF model that describes the susceptibility data (dashed pink line in Fig 11) has a maximum around 300K. This in qualitative agreement with the maximum observed in EPR intensity (Fig. 8c).

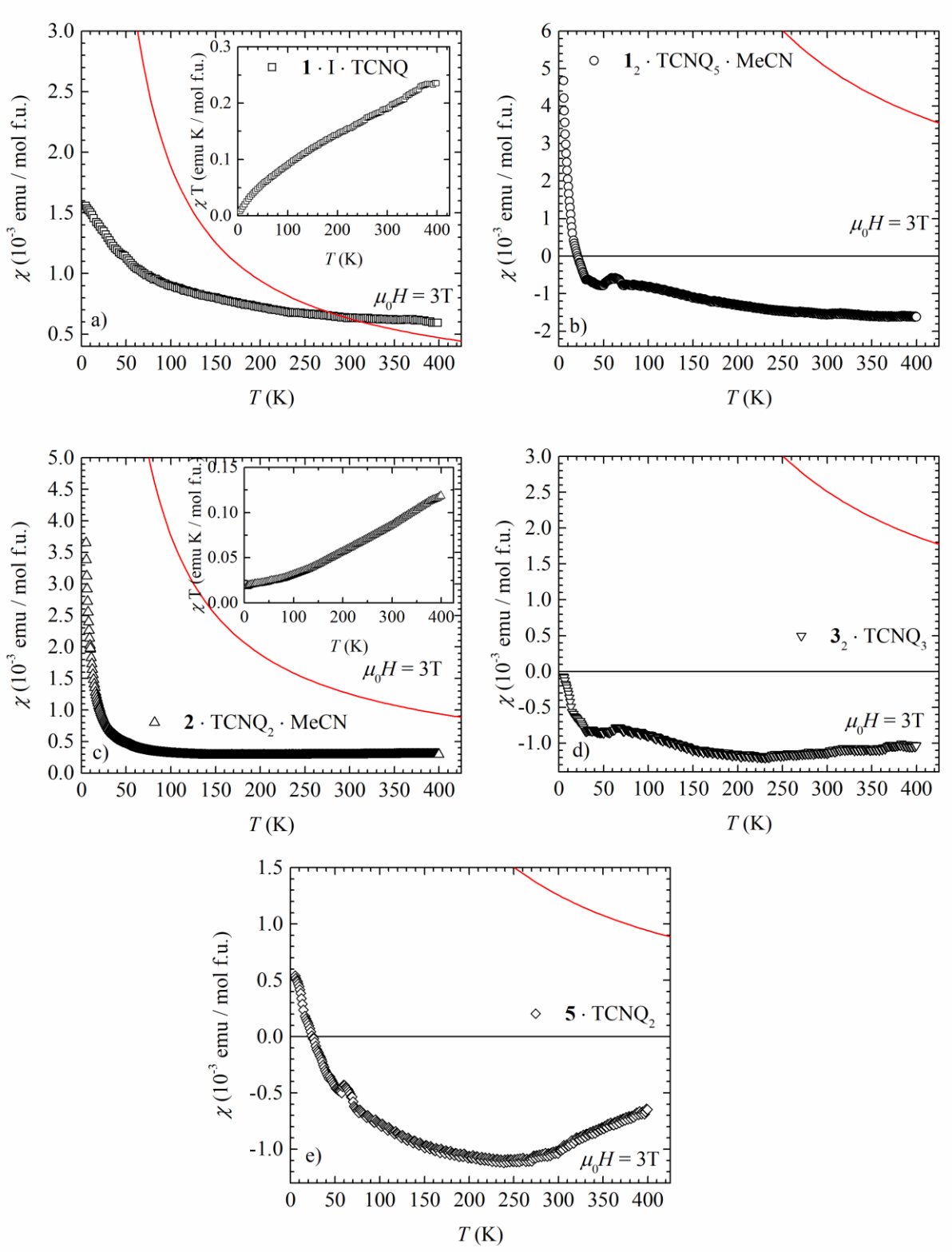

Figure 10 Temperature dependence of magnetic susceptibility measured in μ_0H = 3 T for samples a) **1**·I·TCNQ, b) **1**$_2$·TCNQ$_5$·MeCN, c) **2**·TCNQ$_2$·MeCN, d) **3**$_2$·TCNQ$_3$ and e) **5**·TCNQ$_2$. Solid red

line represents the Curie law which would be obtained for noninteracting spins S = 1/2 where the number of spins per f.u. was calculated under the assumption of formal charges per TCNQ given in the text.

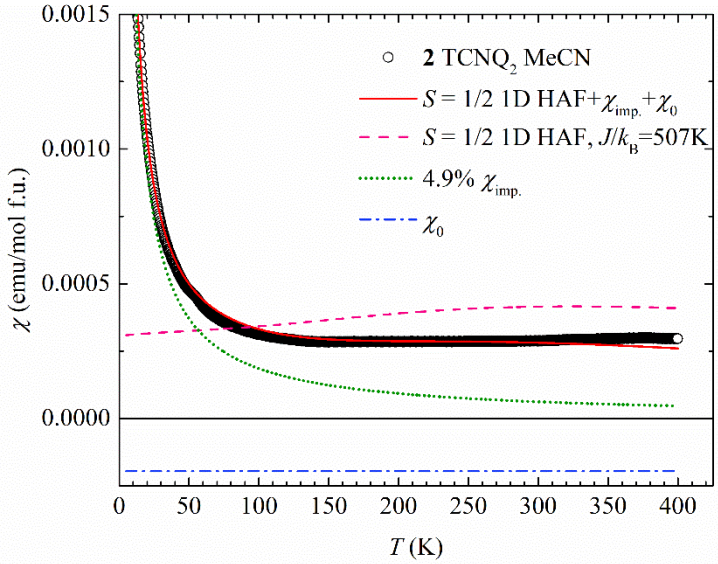

Figure 11 Temperature dependence of susceptibility is well described by the S = 1/2 1D Heisenberg antiferromagnet model with a few percent of spin S = 1/2 impurities (red curve, Eq. 1). The three contributions are also shown separately: pink dashed line - S = 1/2 1D HAF, green dotted line - impurity contribution, blue dash-dotted line - temperature independent diamagnetic contribution.

For other samples, it is not easy to interpret the observed susceptibility data within any model. The observed diamagnetic susceptibility is not in agreement with the EPR results which show a clear presence of unpaired spins. A possible solution to this difference might be the presence of strongly coupled low-dimensional magnetic units which will give weak paramagnetic susceptibility in comparison to the overwhelming diamagnetic contribution. Almost all diamagnetic samples show upturn at the lowest temperatures. However, this upturn cannot be

described as a simple spin $S = 1/2$ impurity contribution, since the M vs H curves with subtracted diamagnetism cannot be described by the $S = 1/2$ Brillouin function (Fig. S24). Extra contribution coming from the underlying antiferromagnetically coupled magnetic structure needs to be added. The possible magnetic structures, however, are not easy to discern, especially considering the complicated charge distribution between the TCNQ moieties. The long-range antiferromagnetic order with weak ferromagnetism is possible for $\mathbf{3}_2{\cdot}TCNQ_3$ and $\mathbf{5}{\cdot}TCNQ_2$, as witnessed from M vs. H curves measured at $T = 5$ K which show significant hysteresis (Fig. S24). However, to obtain more details about the underlying magnetic lattices and possible phase transitions measurements on large-mass single crystal samples are necessary.

CONCLUSIONS

Bulky and non-planar cations cause less efficient packing, large interstices and channels, which may be occupied by iodides or solvent molecules. Therefore, among the six salts studied, two were co-crystallised with solvent molecules, and one is a double salt with iodide. However, this did not affect the formation of pancake bonding, which is present in all studied compounds. This shows that the formation of pancake bonding between radical moieties is very favourable, not only energetically (due to interaction energies exceeding −15 kcal mol^{-1} [1-4], but also due to steric reasons. Therefore, by a smart choice of cation, pancake-bonded motives can be engineered, ranging from 0D (discrete) to 2D (layers).

Since the majority of organic salts of TCNQ comprise aromatic cations, this is the first systematic study of the steric influence of bulky nonaromatic cations on pancake bonding of TCNQ radical anions and involves one of the first salts with an acyclic cation, *N*,*N*,*N*,*N*',*N*',*N*'-hexamethyl-1,2-ethanediaminium.

All the studied samples have unpaired electrons which contribute to the nontrivial magnetic response, as can be seen from sensitive EPR measurements which probe the local magnetic spin-only response. However, only the samples **1**·I·TCNQ and **2**·$TCNQ_2$·MeCN have the total paramagnetic response in the wide temperature range, while $\mathbf{1}_2$·$TCNQ_5$·MeCN, $\mathbf{3}_2$·$TCNQ_3$ and **5**·$TCNQ_2$ are diamagnetic in the wide temperature range. To reconcile this result with the EPR measurements, we conclude that large antiferromagnetic interaction is responsible for the suppression of paramagnetic response with respect to the underlying diamagnetism. Specifically, we show that **2**·$TCNQ_2$·MeCN can be described as $S = 1/2$ 1D Heisenberg antiferromagnet, while $\mathbf{3}_2$·$TCNQ_3$ and **5**·$TCNQ_2$ might have a weakly ferromagnetic long-range-ordered ground state.

EXPERIMENTAL

Preparation and basic characterisation

All used reactants and solvents were purchased from commercial sources (Merck, Sigma-Aldrich, Kemika) with p.a. purity, and were used without further purification.

Studied compounds were prepared according to the previously used and described method for the preparation of salts of semiquinone radicals. [27]

Depending on the solubility of reactants, acetone or acetonitrile was used as a solvent for dissolving reactants and for crystallization. Acetone was used as a solvent for crystallisation of $\mathbf{3}_2$·$TCNQ_3$ while acetonitrile was used for crystallization of **1**·I·TCNQ, $\mathbf{1}_2$·$TCNQ_5$·MeCN, **2**·$TCNQ_2$·MeCN, **4**·$TCNQ_3$ and **5**·$TCNQ_3$. Powdered TCNQ (10 mg) was dissolved in adequate cold solvent until the saturation of the solution. Approximately 50% excess of the iodide salt of the appropriate cation was added into the prepared TCNQ solution to ensure the oxidation of dissolved TCNQ into its anion radical. If needed, more solvent was added to dissolve all reactants

(maximum 15 ml, 5˚C). Furthermore, to enhance the reaction, more iodide was added in form of tetrabutylamoniun iodide (approximately 10 mg) to the crystallization mixture of TCNQ with **1**·I·TCNQ/**1**$_2$·TCNQ$_5$·MeCN and **4**·TCNQ$_3$. The beaker with prepared solution was sealed with parafilm with pierced holes. After 1−3 days single crystals were obtained, the solution was decanted and black crystals of radical salts were extracted. **1**·I·TCNQ and **1**$_2$·TCNQ$_5$·MeCN crystallized from the same preparation. Prepared compounds are stable in air at room temperature for more than 6 months.

EPR spectroscopy

Electron paramagnetic resonance (EPR) spectroscopy measurements were performed on the benchtop Bruker Magnettech ESR5000 spectrometer (Bruker BioSpin, Germany) equipped with a TCH04 variable temperature controller (Bruker BioSpin, Germany) using a flow of cold N_2 steam. The powder EPR spectra were recorded in the temperature range of 120–400 K. A Bruker standard reference E1704, Mn^{2+} in ZnS, was used to calibrate the magnetic field and to determine the exact *g*-values of the samples.

The spectra were simulated with a custom program in MATLAB [42] using the Easyspin program package for EPR [43].

Magnetization measurements

Magnetization measurements were performed using SQUID VSM option of Quantum Design (QD) MPMS3 magnetometer. The powder samples of mass 1.087 mg, 1.146 mg, 10.4 mg, 0.849 mg and 0.646 mg for **1**·I·TCNQ, **1**$_2$·TCNQ$_5$·MeCN, **2**·TCNQ$_2$·MeCN, **3**$_2$·TCNQ$_3$ and **5**·TCNQ$_2$ respectively, were mounted inside a standard QD powder capsule attached to the standard QD

brass sample holder. The temperature dependence was measured in the temperature range 5 − 400 K in magnetic fields up to $\mu_0 H$ = 3 T, and the magnetic field dependence of magnetization was measured in fields up to ± 7 T.

X-ray diffraction

Single crystal measurements for **1**·I·TCNQ and $\mathbf{1}_2$·$TCNQ_5$·MeCN and **5**·$TCNQ_2$ were performed on an Oxford Diffraction Xcalibur Nova R (microfocus Cu tube) equipped with an Oxford Instruments CryoJet cryostat and for **2**·$TCNQ_2$·MeCN on a dual source (Mo/Cu) Rigaku Oxford Diffraction Synergy S diffractometer equipped with an Oxford Cryosystems Series 800 cryostat. The program package CrysAlis PRO [44] was used for data reduction and numerical absorption correction. Single-crystal X-ray diffraction data for $\mathbf{3}_2$·$TCNQ_3$ were collected at the Rossendorf Beamline (ESRF / Grenoble, France) [45] equipped with a Si(111) monochromator and two Pt coated mirrors. The single-crystal data were recorded with a Pilatus3 X 2M detector (Dectris) with an excitation energy of 20000 eV / wavelength 0.6200926 Å. The monochromator energy was calibrated against the first inflection point of the *K*-absorption edge of a Mo metal foil, tabulated as 20000 eV. The diffraction measurements were performed in shutterless mode with an angular step size of 0.1° and a counting time of 0.1s per frame. The detector geometry parameters were calibrated with *PyFAI* [46] using a powder pattern of the NIST 660c standard LaB_6. Experimental data were collected using the *Pylatus* software [47] and treated using the *SNBL ToolBox* [47] and *CrysAlisPro* [44].

The structures were solved using SHELXS97 [48] and refined with SHELXL-2017 [49]. Models were refined using the full-matrix least squares refinement; all non-hydrogen atoms were refined anisotropically. Hydrogen atoms were located in a difference Fourier map and refined as riding

entities. In **2**·$TCNQ_2$·MeCN an acetonitrile molecule is disordered about an inversion centre, so it was refined using geometric and rigid-body restraints. The crystals of $\mathbf{3}_2$·$TCNQ_3$ are twinned according to a twin law $\begin{bmatrix} 1 & 0 & 1 \\ 0 & -1 & 0 \\ 0 & 0 & -1 \end{bmatrix}$, so the structure was refined as a twin with 18 % of the minor component. The data were cut off at 0.80 Å as data quality was insufficient above this threshold.

Molecular geometry calculations were performed by PLATON [50] and molecular graphics were prepared using ORTEP-3 [51], and Mercury [52]. Crystallographic and refinement data for the structures reported in this paper are shown in Table 5.

Table 5 Crystallographic, data collection and refinement data.

Compound	$\mathbf{1}_2$·$TCNQ_5$·MeCN	**1**·I·TCNQ	**2**·$TCNQ_2$·MeCN	$\mathbf{3}_2$·$TCNQ_3$
Empirical formula	$C_{78}H_{59}N_{25}$	$C_{20}H_{16}IN_6$	$C_{36}H_{30}N_{12}$	$C_{74}H_{42}N_{20}$
Formula wt. / g mol^{-1}	1346.5	467.29	630.72	1211.28
Colour	black	black	black	black
Crystal dimensions / mm	0.40 x 0.33 x 0.12	0.30 x 0.28 x 0.06	0.21 x 0.13 x 0.06	0.08 x 0.02 x 0.01
Space group	$P\bar{1}$	$C\,2/c$	$I\,2/m$	$P\,2_1/c$
a / Å	7.8050(2)	8.1193(3)	10.1504(3)	29.0602(6)
b / Å	13.4525(5)	13.5467(5)	6.4646(2)	11.5161(3)
c / Å	16.7606(6)	19.0588(9)	26.7934(8)	19.7924(6)
α / °	80.776(3)	90	90	90
β / °	81.830(2)	99.593(4)	98.494(3)	109.859(3)
γ / °	83.955(2)	90	90	90

Z	1	4	2	2
V / Å^3	1713.28(10)	2066.96(15)	1738.85(9)	6229.8(3)
D_{calc} / g cm^{-3}	1.305	1.502	1.205	1.291
λ / Å	1.54179 (Cu$K\alpha$)	1.54179 (Cu$K\alpha$)	1.54179 (Cu$K\alpha$)	0.56356
μ / mm^{-1}	0.664	12.298	0.613	0.053
Θ range / °	3.34 – 75.77	4.71 - 75.96	3.34 - 79.38	1.52 – 40.67
T / K	293(1)	293(2)	293(2)	100(2)
Diffractometer type	Xcalibur Nova	Xcalibur Nova	Synergy S	Pilatus3 X 2M
Range of h, k, l	-7 < h < 9; -16 < k < 15; -21 < l < 20	-10 < h < 9; -16 < k < 13; -22 < l < 23	-12 < h < 12; -8 < k < 6; -33 < l < 33	–66 < h < 66; –26 < k < 26; –45 < l < 45
Reflections collected	16581	5425	11731	439755
Independent reflections	8648	2127	2039	11124
Observed reflections ($I \geq 2\sigma$)	8321	1898	1821	10370
Absorption correction	Multi-scan	Multi-scan	Multi-scan	Multi-scan
T_{min}, T_{max}	0.8754; 1.0000	0.1329; 1.0000	0.5061; 1.0000	0.7800; 1.0000
R_{int}	0.0191	0.0520	0.0338	0.0758
R (F)	0.0372	0.0640	0.1295	0.0696
R_w (F^2)	0.1130	0.1905	0.4346	0.2250
Goodness of fit	1.012	1.051	2.067	0.851
H atom treatment	Mixed	Constrained	Constrained	Constrained
No. of parameters	937	123	133	848

No. of restraints	8	0	0	0
$\Delta\rho_{max}$, $\Delta\rho_{min}$ (eÅ^{-3})	0.169; -0.149	1.639; -0.761	0.994; -0.688	0.499; −0.384

Table 5 Cont'd.

Compound	**4**·$TCNQ_3$	**5**·$TCNQ_2$
Empirical formula	$C_{47}H_{24}N_{14}$	$C_{36}H_{16}I_2N_9$
Formula wt. / g mol^{-1}	784.80	828.38
Colour	black	black
Crystal dimensions / mm	0.40 x 0.31 x 0.24	0.35 x 0.05 x 0.04
Space group	*C m*	$P\bar{1}$
a / Å	7.7355(3)	6.6609(2)
b / Å	19.2004(8)	16.3488(5)
c / Å	13.2123(6)	17.1075(7)
α / °	90	61.533(4)
β / °	91.810(4)	82.226(3)
γ / °	90	80.160(2)
Z	2	2
V / Å^3	1961.37(14)	1610.51(11)
D_{calc} / g cm^{-3}	1.329	1.708
λ / Å	1.54179 (Cu*K*α)	1.54179 (Cu*K*α)
μ / mm^{-1}	0.679	15.673
Θ range / °	3.35 – 79.58	2.94 – 76.48

T / K	293(2)	293(2)
Diffractometer type	Synergy S	Xcalibur Nova
Range of h, k, l	$-9 < h < 9$; $-24 < k < 22$; $-16 < l < 15$	$-8 < h < 7$; $-19 < k < 20$; $-21 < l < 21$
Reflections collected	7848	14741
Independent reflections	3289	6639
Observed reflections ($I \geq 2\sigma$)	3011	6165
Absorption correction	Multi-scan	Multi-scan
T_{min}, T_{max}	0.3290; 1.0000	0.0561; 1.0000
R_{int}	0.0227	0.0498
R (F)	0.0524	0.0544
R_w (F^2)	0.1619	0.1534
Goodness of fit	0.849	0.959
H atom treatment	Constrained	Constrained
No. of parameters	301	424
No. of restraints	2	0
$\Delta\rho_{max}$, $\Delta\rho_{min}$ (eÅ^{-3})	0.308; -0.242	1.823; -2.085

ASSOCIATED CONTENT

Supporting Information. ORTEP diagrams, geometry and charge of TCNQ moieties, EPR results, magnetization measurements. This material is available free of charge via the Internet at http://pubs.acs.org.

AUTHOR INFORMATION

Corresponding Author

*e-mail: kmolcano@irb.hr

Author Contributions

The manuscript was written through the contributions of all authors. All authors have given approval to the final version of the manuscript.

Funding Sources

This work was supported by the Croatian Science Foundation, grant IP-2019-04-4674, project Cryogenic Centre at the Institute of Physics - KaCIF (Grant KK.01.1.1.02.0012), co-financed by the Croatian Government and the European Union through the European Regional Development Fund – Competitiveness and Cohesion Operational Programme and the project Ground states in competition – strong correlations, frustration and disorder — FrustKor financed by the Croatian Government and the European Union through the National Recovery and Resilience Plan 2021-2026 (NPOO). Financial support by German-Croatian bilateral collaboration (DAAD-MZOS) is gratefully acknowledged. F.M. thanks the Studienstiftung des Deutschen Volkes for a PhD fellowship.

ABBREVIATIONS

CCR2, CC chemokine receptor 2; CCL2, CC chemokine ligand 2; CCR5, CC chemokine receptor 5; TLC, thin layer chromatography.

REFERENCES

(Word Style “TF_References_Section”). References are placed at the end of the manuscript. Authors are responsible for the accuracy and completeness of all references. Examples of the recommended format for the various reference types can be found at http://pubs.acs.org/page/4authors/index.html. Detailed information on reference style can be found in *The ACS Style Guide,* available from Oxford Press.

[1] M. Kertesz, (2018) *Chem. Eur. J.*, **25**, 400-416.

[2] K. E. Preuss, *Polyhedron*, **79** (2014), 1-15.

[3] K. Molčanov, B. Kojić-Prodić, *IUCrJ*, **6** (2019), 156-166.

[4] K. Molčanov, V. Milašinović, B. Kojić-Prodić, *Cryst. Growth Des.*, **19** (2019), 5967-5980.

[5] T. Steiner, *Angew. Chem., Int. Ed.*, 2002, **41**, 48-76.

[6] B. Kojić-Prodić, K. Molčanov, *Acta Chim. Slov.*, 2008, **55**, 692-708.

[7] V. Stilinović, G. Horvat, T. Hrenar, V. Nemec, D. Cinčić, *Chem. Eur. J.* **2017**, *23*, 5244–5257.

[9] M. Eraković, D. Cinčić, K. Molčanov, V. Stilinović, *Angew. Chem., Int. Ed.*, **58** (2019), 15702-15706.

[9] Hicks, R. G., *Nature Chem.*, **2011**, *3*, 189–191.

[10] Sanvito, S., *Chem. Soc. Rev.*, **2011**, *40*, 3336–3355.

[11] Podzorov, V., *Nature Mater.*, **2010**, *10*, 616–617.

[12] Sanvito, S., *Nature Mater.*, **2011**, *10,* 484–485.

[13] Veciana, J. (ed.), π-Electron magnetism: From molecules to magnetic materials, in *Struct. Bond.*, **2011**, *100*.

[14] Morita, Y.; Murata, T.; Nakasuji, K. (2013) *Bull. Chem. Soc. Jpn*, **86**, 183-197.

[15] Murata, T.; Yamamoto, Y.; Yakiyama, Y.; Nakasuji, K.; Morita, Y. (2013) *Bull. Chem. Soc. Jpn*, **86**, 927-939.

[16] Ratera, I.; Veciana, J., *Chem. Soc. Rev.*, **2011**, *40*, 303–349.

[17] K. Molčanov, V. Stilinović, A. Šantić, N. Maltar-Strmečki, D. Pajić, B. Kojić-Prodić, *Cryst. Growth Des.*, **16** (2016), 4777-4782.

[18] K. Molčanov, D. Stalke, A. Šantić, S. Demeshko, V. Stilinović, Z. Mou, M. Kertesz, B. Kojić-Prodić, *CrystEngComm*, **20** (2018), 1862-1873.

[19] P. Stanić, D. Barišić, D. Pajić, A. Šantić, K. Molčanov, *Cryst. Growth Des.*, **22** (2022), 6461-6471.

[20] Mercuri, M. L.; Deplano, P.; Pilia, L.; Serpe, A.; Artizzu, F. (2010) *Coord. Chem. Rev.*, **254**, 1419-1433.

[21] T. Nakano, Edt. *π-Stacked Polymers and Molecules*, Springer **2014**.

[22] Lekin, K.; Winter, S. M.; Downie, L. E.; Bao, X.; Tse, J. S.; Desgreniers, S.; Secco, R. A.; Dube, P. A.; Oakley, R. T., *J. Am. Chem. Soc.*, **2010**, *132*, 16212–16224.

[23] Yu, X.; Mailman, A.; Dube, P. A.; Assoud A.; Oakley, R. T., *Chem. Commun.*, **2011**, 4655–4657.

[24] Yu, X.; Mailman, A.; Lekin, K.; Assoud, A.; Robertson, C. M.; Noll, B. C.; Campana, C. F.; Howard, J. A. K.; Dube, P. A.; Oakley, R. T., *J. Am. Chem. Soc.*, **2012**, *134*, 2264–2275.

[25] X. Chen, F. Gao, W. Yang, Sci. Rep. 2016, **6** : 29314 doi:10.1038/srep29314 (2016).

[26] P. Alemany, E. Canadell, Y. Geng, J. Hauser, P. Macchi, K. Krämer, S. Decurtins, S.-X. Liu, *ChemPhysChem*, 2015, **16**, 1361-1365.

[27] K. Molčanov, V. Milašinović, B. Kojić-Prodić, N. Maltar-Strmečki, J. You, A. Šantić, L. Kanižaj, V. Stilinović, L. Fotović, *IUCrJ*, **9** (2022), 449-467.

[28] T. J. Kistenmacher, T. J. Emge, A. N. Bloch, D. O. Cowan, *Acta Cryst. B*, **B38** (1982), 1193-1199.

[29] K. Molčanov, V. Milašinović, N. Ivić, D. Kolarić, B. Kojić-Prodić, *CrystEngComm*, **21** (2019), 6920-6928.

[30] F. H. Herbtein & M. Kapon, *Crystallogr. Rev.*, **14** (2008), 3-74.

[31] K. Molčanov, Z. Mou, M. Kertesz, B. Kojić-Prodić, D. Stalke, S. Demeshko, A. Šantić, V. Stilinović, *Chem. Eur. J.*, **24** (2018), 8292-8297.

[32] Coulon, C.; Clerac, R., Electron Spin Resonance: A Major Probe for Molecular Conductors, *Chem. Rev.*, **2004**, *104*, 5655-5687.

[33] Bain, G. A.; Berry, J. F., Diamagnetic Corrections and Pascal's Constants, *J. Chem. Educ.*, **2008**, *85*, 532-536.

[34] Johnston, D. C.; Kremer, R. K.; Troyer, M.; Wang, X.; Kluemper, A.; Budko, S. L.; Panchula, A. F.; Canfield, P. C., Thermodynamics of spin S=1/2 antiferromagnetic uniform and alternating-exchange Heisenberg chains, *Phys. Rev. B*, **2000**, *61*, 9558-9606.

[35] Scott, J. C.; Garito, A. F.; Heeger, A. J., Magnetic susceptibility studies of tetrathiofulvalene-tetracyanoquinodimethan (TTF) (TCNQ) and related organic metals, *Phys. Rev. B,* **1974**, *10,* 3131-3139.

[36] Dzyaloshinskii, I., A thermodynamic theory of 'weak' ferromagnetism or antiferromagnetics, *J. Phys. Chem. Solids,* **1958**, *4*, 241-255.

[37] Moriya, T., Anisotropic Superexchange Interaction and Weak Ferromagnetism, *Phys. Rev.*, **1960**, *120*, 91-98.

[38] Oshikawa, M.; Affleck, I., Field-Induced Gap in *S*=1/2 Antiferromagnetic Chains, *Phys. Rev. Lett.*, **1997**, *79* 2883-2886.

[39] Affleck, I.; Oshikawa, M., Field-induced gap in Cu benzoate and other *S*=1/2 antiferromagnetic chains, *Phys. Rev. B*, **1999**, *60*, 1038-1056.

[40] Affleck, I.; Oshikawa, M., Erratum: Field-induced gap in Cu benzoate and other *S*=1/2 antiferromagnetic chains [Phys. Rev. B **60**, 1038 (1999)], *Phys. Rev. B*, **2000**, *62*, 9200-9200.

[41] Herak, M.; Zorko, A.; Arčon, D.; Potočnik, A.; Klanjšek, M.; van Tol, J.; Ozarowski, A.; Berger, H., Symmetric and antisymmetric exchange anisotropies in quasi-one-dimensional CuSe2O5 as revealed by ESR, *Phys. Rev. B*, **2011**, *84*, 184436.

[42] The MathWorks Inc. (**2022**). *MATLAB* version: 9.13.0 (R2022b), Natick, Massachusetts: The MathWorks Inc. https://www.mathworks.com

[43] Stoll, S.; Schweiger, A. EasySpin, a comprehensive software package for spectral simulation and analysis in EPR, *J. Magn. Reson.*, **2006**, *178*, 42-55.

[44] O.D. Rigaku, P.R.O. CrysAlis, version: V.40, Rigaku Oxford Diffraction Ltd, Yarnton, England, **2021**.

[45] Scheinost, A. C.; Claussner, J.; Exner, J.; Feig, M.; Findeisen, S.; Hennig, C.; Kvashnina, K. O.; Naudet, D.; Prieur, D.; Rossberg, A.; Schmidt, M.; Qiu, C.; Colomp, P.; Cohen, C.; Dettona, E.; Dyadkin, V.; Stumpf T. ROBL-II at ESRF: a synchrotron toolbox for actinide research, *J. Synchr. Rad*., **2021**, *28*, 333-349.

[46] Kieffer J.; Wright, J. P. PyFAI: a Python library for high performance azimuthal integration on GPU, *Powder Diffraction*, **2013**, *28*, S339-S350.

[47] Dyadkin, V.; Pattison, P.; Dimitriev V.; Chernyshov, D. A new multipurpose diffractometer PILATUS@SNBL, *J. Synchrotron Rad*., **2016**, *23*, 825-829.

[48] Sheldrick, G. M. *SHELXT* - Integrated Space-Group and Crystal-Structure Determination. *Acta Crystallogr. A*. **2015**, A71, 3-8.

[49] Sheldrick, G. M. Crystal structure refinement with SHELXL. *Acta Crystallogr. C*, **2015**, C71, 3–8.

[50] Spek, A. L. *checkCIF* validation ALERTS: what they mean and how to respond, *Acta Grystallogr. E*, **2020**, *E76*, 1-11.

[51] Farrugia, L. J. *ORTEP*-3 for Windows - a version of *ORTEP*-III with a Graphical User Interface (GUI). *J. Appl. Crystallogr.* **1997**, 30, 565.

[52] Macrae, C. F., Sovago, I., Cottrell, S. J., Galek, P. T. A., McCabe, P., Pidcock, E., Platings, M., Shields, G. P., Stevens, J. S., Towler, M. & Wood, P. A. Mercury 4.0: from visualization to analysis, design and prediction. *J. Appl. Crystallogr.* **2020**, 53, 226-235.

[53] Molčanov, K.; Kojić-Prodić, B. Spin pairing, electrostatic and dipolar interactions influence stacking of radical anions in alkali salts of 4,5-dichloro-3,6-dioxocyclohexa-1,4-diene-1,2-dicarbonitrile (DDQ), *CrystEngComm*, **2017**, *19*, 1801-1808.

Insert Table of Contents Graphic and Synopsis Here

The influence of sterically bulky cations on the packing efficiency of TCNQ radical salts is studied, and it is shown that the formation of pancake bonding between TCNQ radicals is not hindered. Different arrays of stacked TCNQ, ranging from 0D to 2D are.

Structural variety of extended arrays of pancake-bonded TCNQ radicals: steric effect of the bulky cations

Petra Stanić,[a] Kristina Smokrović,[a] Nadica Maltar-Strmečki,[a] Mirta Herak,[b] Florian Meurer,[c,d] Michael Bodensteiner,[c] Christoph Hennig[d,e] and Krešimir Molčanov*[a]

a Ruđer Bošković Institute, Bijenička c. 54, HR-10000 Zagreb, Croatia

b Institute of Physics, Bijenička c. 46, HR-10000 Zagreb, Croatia

c Universität Regensburg, Universitätsstrasse 31, 93053 Regensburg, Germany

d Helmholtz-Zentrum Dresden-Rossendorf, Institute of Resource Ecology, Bautzner Landstraße 400, 01314 Dresden, Germany

e The Rossendorf Beamline (BM20), European Synchrotron Radiation Facility, 71 Avenue des Martyrs, 38043 Grenoble, France

e-mail: kmolcano@irb.hr

S1 ORTEP drawings

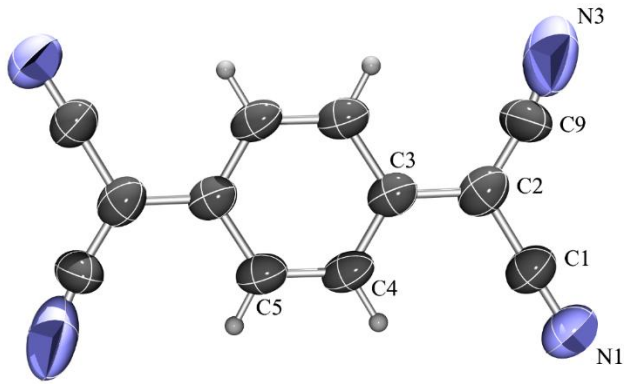

Figure S1 ORTEP drawing of TCNQ moiety in **1**·I·TCNQ with atom labelling scheme. Displacement ellipsoids are drawn for the probability of 50 % and hydrogen atoms are shown as spheres of arbitrary radii.

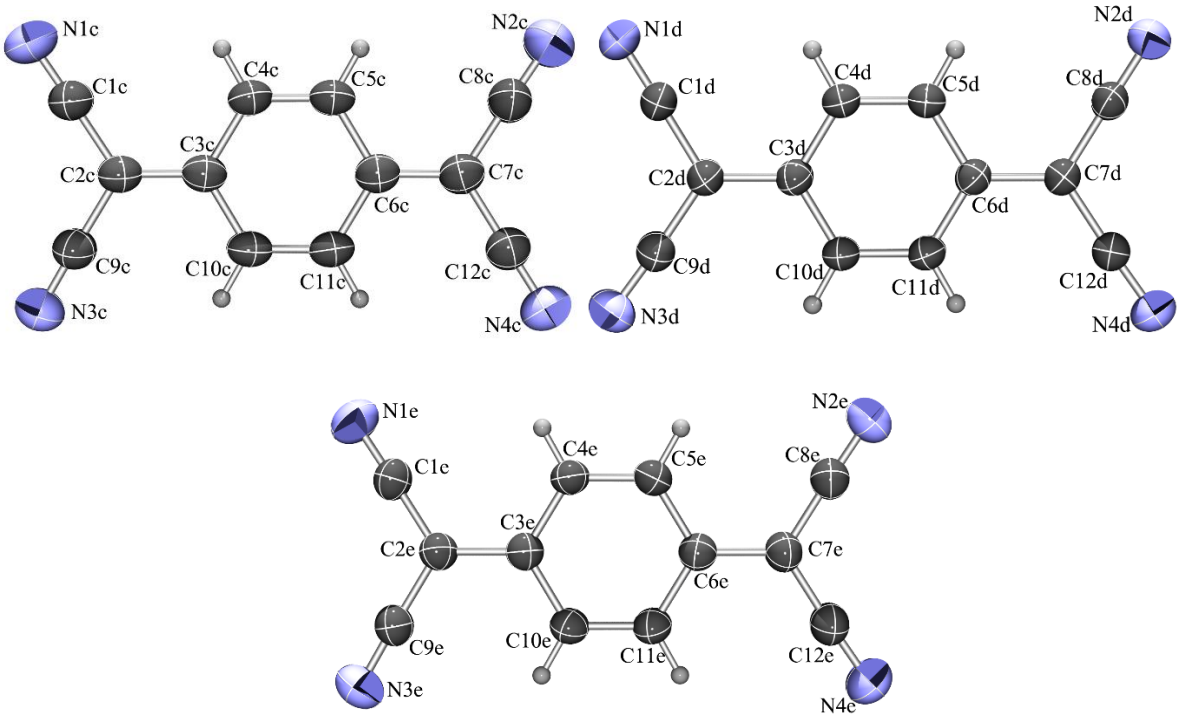

Figure S2 ORTEP drawing of five symmetry-independent TCNQ moieties in **1**$_2$·TCNQ$_5$·MeCN with atom labelling scheme. Displacement ellipsoids are drawn for the probability of 50 % and hydrogen atoms are shown as spheres of arbitrary radii.

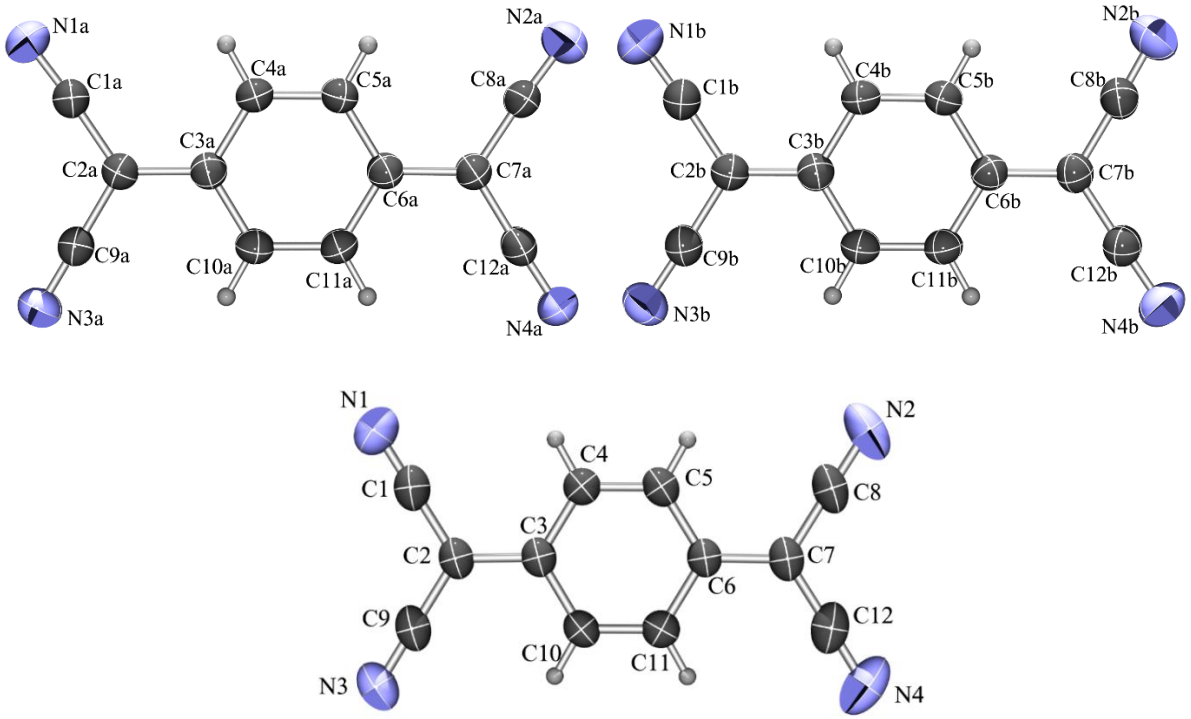

Figure S3 ORTEP drawing of TCNQ moiety in **2**·TCNQ$_2$·MeCN with atom labelling scheme. Displacement ellipsoids are drawn for the probability of 50 % and hydrogen atoms are shown as spheres of arbitrary radii.

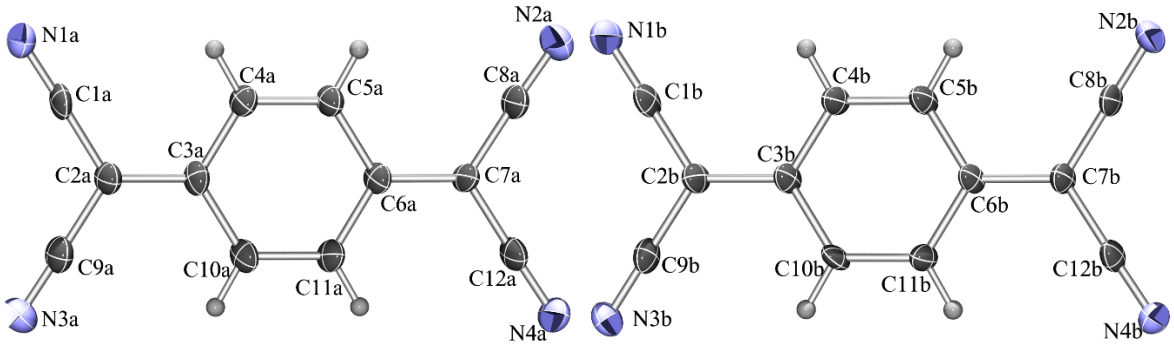

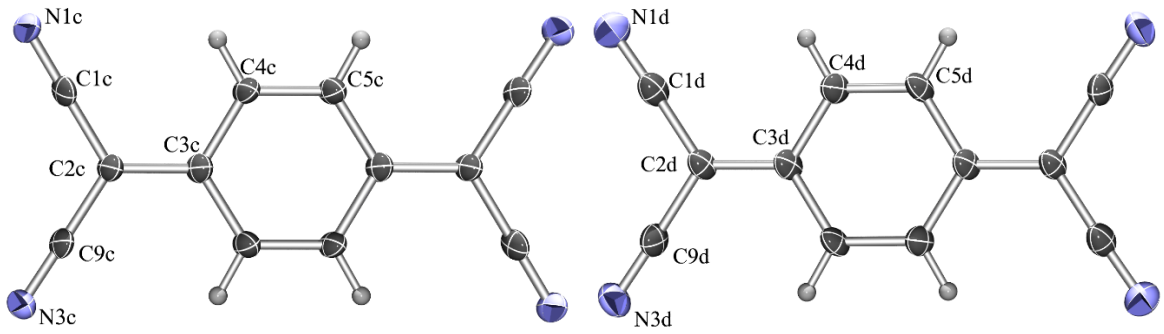

Figure S4 ORTEP drawing of four symmetry-independent TCNQ moieties in $\mathbf{3}_2$·$TCNQ_3$ with atom labelling scheme. Displacement ellipsoids are drawn for the probability of 50 % and hydrogen atoms are shown as spheres of arbitrary radii.

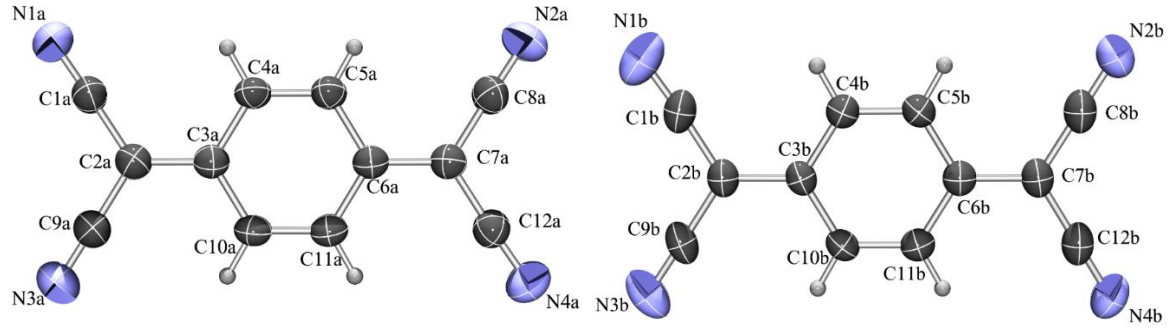

Figure S5 ORTEP drawing of two symmetry-independent TCNQ moieties in **4**·$TCNQ_3$ with atom labelling scheme. Displacement ellipsoids are drawn for the probability of 50 % and hydrogen atoms are shown as spheres of arbitrary radii.

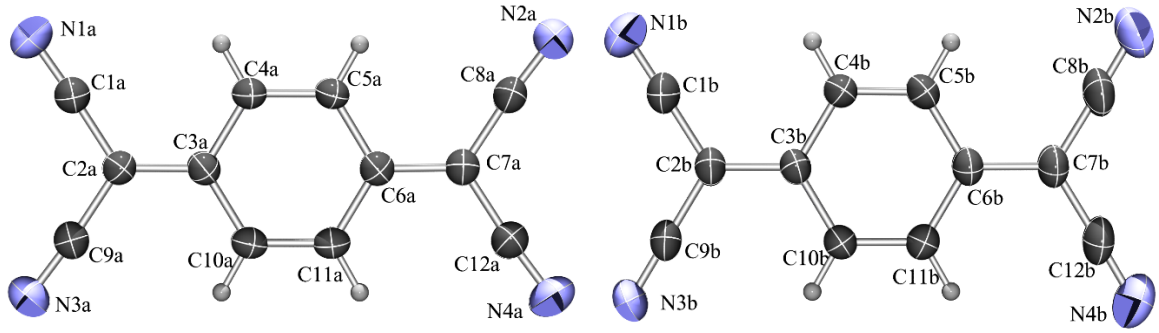

Figure S6 ORTEP drawing of two symmetry-independent TCNQ moieties in **5**·$TCNQ_2$ with atom labelling scheme. Displacement ellipsoids are drawn for the probability of 50 % and hydrogen atoms are shown as spheres of arbitrary radii.

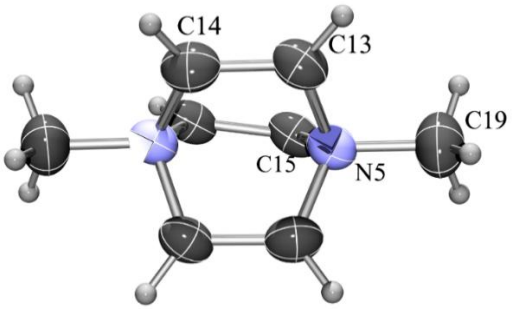

Figure S7 ORTEP drawing of **1** cation in **1**·I·TCNQ with atom labelling scheme. Displacement ellipsoids are drawn for the probability of 50 % and hydrogen atoms are shown as spheres of arbitrary radii.

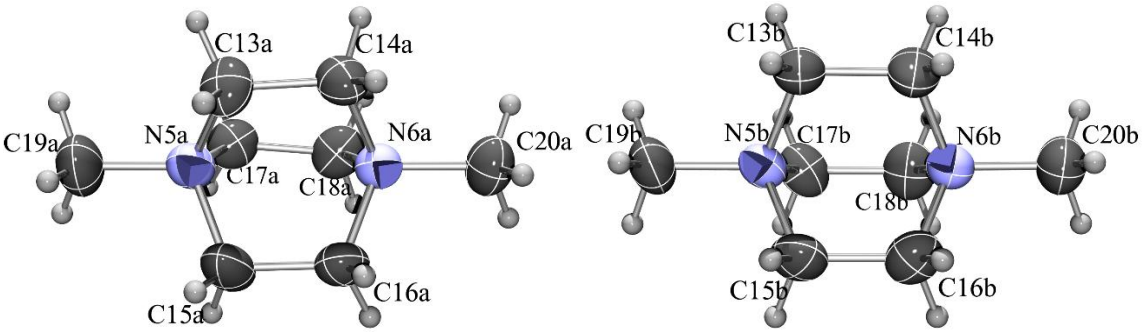

Figure S8 ORTEP drawing of two symmetry-independent **1** cations in **1**$_2$·$TCNQ_5$·MeCN with atom labelling scheme. Displacement ellipsoids are drawn for the probability of 50 % and hydrogen atoms are shown as spheres of arbitrary radii.

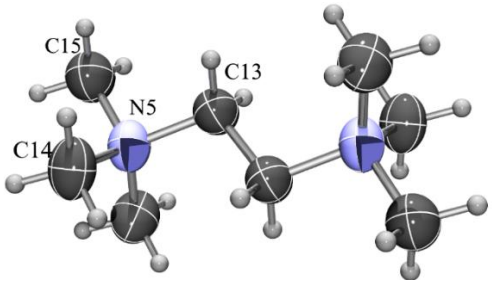

Figure S9 ORTEP drawing of **2** cation in **2**·$TCNQ_2$·MeCN with atom labelling scheme. Displacement ellipsoids are drawn for the probability of 50 % and hydrogen atoms are shown as spheres of arbitrary radii.

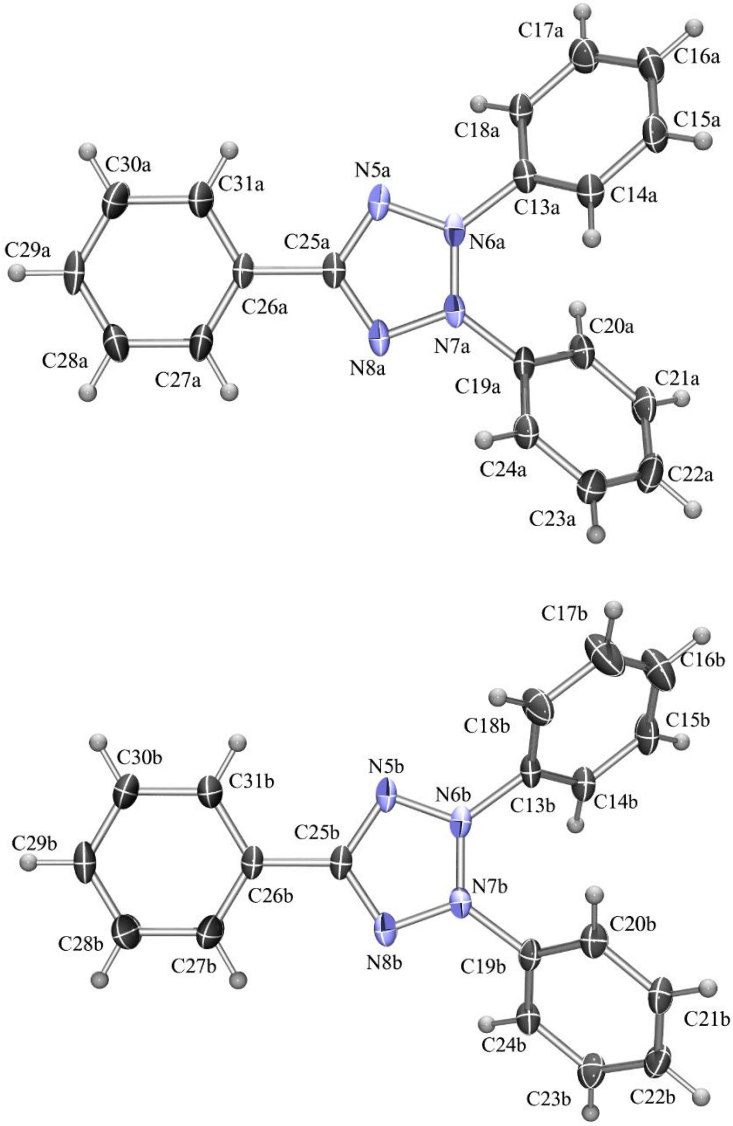

Figure S10 ORTEP drawing of two symmetry-independent tetrazolium cations in $\mathbf{3}_2$·$TCNQ_3$ with atom labelling scheme. Displacement ellipsoids are drawn for the probability of 50 % and hydrogen atoms are shown as spheres of arbitrary radii.

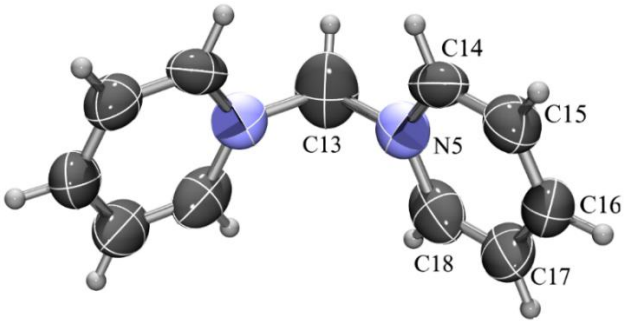

Figure S11 ORTEP drawing of **4** cation in **4**·$TCNQ_3$ with atom labelling scheme. Displacement ellipsoids are drawn for the probability of 50 % and hydrogen atoms are shown as spheres of arbitrary radii.

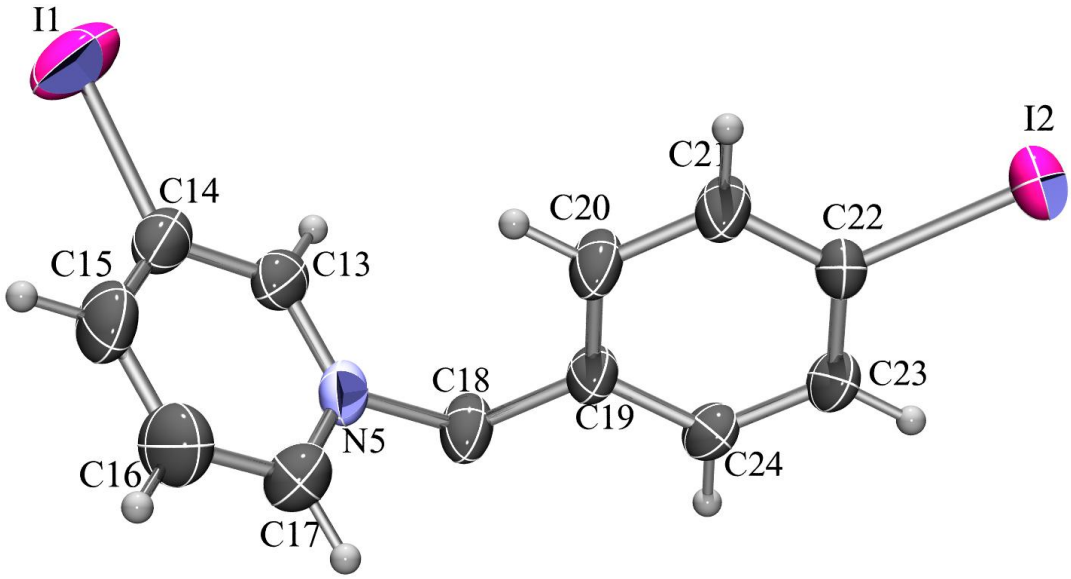

Figure S12 ORTEP drawing of **5** cation in **5**·$TCNQ_2$ with atom labelling scheme. Displacement ellipsoids are drawn for the probability of 50 % and hydrogen atoms are shown as spheres of arbitrary radii.

S2 Geometry of TCNQ moieties

Table S1 Bond lengths in TCNQ radicals (Å). Only symmetry-independent bonds are listed.

	$\mathbf{1}_2$·$TCNQ_5$· MeCN **A**	$\mathbf{1}_2$·$TCNQ_5$ ·MeCN **B**	$\mathbf{1}_2$·$TCNQ_5$· MeCN **C**	$\mathbf{1}_2$·$TCNQ_5$· MeCN **D**	$\mathbf{1}_2$·$TCNQ_5$· MeCN **E**	**1**·I·TCNQ	**2**·$TCNQ_2$· MeCN
C1-C2	1.415(3)	1.418(3)	1.436(3)	1.416(3)	1.418(3)	1.435(13)	1.425(6)
C2-C3	1.421(3)	1.404(3)	1.377(3)	1.417(3)	1.417(3)	1.422(12)	1.414(5)
C2-C9	1.410(3)	1.424(3)	1.430(3)	1.412(3)	1.410(3)	1.287(14)	1.407(6)
C3-C4	1.423(3)	1.433(3)	1.442(3)	1.423(3)	1.423(3)	1.391(10)	1.418(6)
C3-C10	1.420(3)	1.423(3)	1.437(3)	1.417(3)	1.425(3)	1.420(11)	1.429(6)
C4-C5	1.366(3)	1.352(3)	1.345(3)	1.359(3)	1.360(3)	1.353(12)	1.353(5)
C5-C6	1.415(3)	1.432(3)	1.443(3)	1.425(3)	1.424(3)		1.424(6)
C6-C7	1.421(3)	1.405(3)	1.374(3)	1.416(3)	1.407(3)		1.403(5)
C6-C11	1.421(3)	1.428(3)	1.444(3)	1.409(3)	1.425(3)		1.432(6)
C7-C8	1.416(3)	1.423(3)	1.432(4)	1.416(3)	1.416(3)		1.418(6)
C7-C12	1.403(3)	1.416(3)	1.428(3)	1.413(3)	1.417(4)		1.397(6)
C10-C11	1.362(3)	1.361(3)	1.343(3)	1.368(3)	1.363(3)		1.361(5)
C1-N1	1.151(3)	1.147(3)	1.138(3)	1.151(3)	1.157(3)	1.144(14)	1.147(7)
C8-N2	1.152(3)	1.144(4)	1.135(4)	1.150(3)	1.148(3)	1.10(3)	1.171(8)
C9-N3	1.154(3)	1.147(3)	1.142(3)	1.154(3)	1.149(3)		1.162(6)
C12-N4	1.147(3)	1.145(3)	1.141(3)	1.148(3)	1.151(4)		1.155(8)

Table S1 Cont'd.

	3$_2$·TCNQ$_3$ **A**	**3**$_2$·TCNQ$_3$ **B**	**3**$_2$·TCNQ$_3$ **C**	**3**$_2$·TCNQ$_3$ **D**	**4**·TCNQ$_3$ **A**	**4**·TCNQ$_3$ **B**
C1-C2	1.433(4)	1.421(4)	1.428(4)	1.443(4)	1.428(4)	1.424(5)
C2-C3	1.401(4)	1.422(4)	1.418(4)	1.386(4)	1.394(4)	1.407(6)
C2-C9	1.434(4)	1.425(4)	1.426(4)	1.436(4)	1.422(5)	1.415(6)
C3-C4	1.431(4)	1.420(4)	1.438(4)	1.441(4)	1.428(4)	1.425(5)
C3-C10	1.443(4)	1.440(4)	1.420(4)	1.448(4)	1.436(3)	1.434(5)
C4-C5	1.364(4)	1.366(4)	1.369(4)	1.362(4)	1.354(4)	1.361(6)
C5-C6	1.436(4)	1.431(4)			1.441(3)	1.428(5)
C6-C7	1.398(4)	1.415(4)			1.389(4)	1.405(6)
C6-C11	1.434(4)	1.434(4)			1.429(4)	1.435(5)
C7-C8	1.434(4)	1.426(4)			1.417(5)	1.417(6)
C7-C12	1.425(4)	1.430(4)			1.420(4)	1.420(6)
C10-C11	1.367(4)	1.366(4)			1.355(4)	1.364(6)
C1-N1	1.161(4)	1.168(4)	1.154(4)	1.157(4)	1.139(4)	1.143(7)
C8-N2	1.152(4)	1.160(4)			1.148(5)	1.153(6)
C9-N3	1.152(4)	1.159(4)	1.162(4)	1.155(4)	1.142(5)	1.149(7)
C12-N4	1.164(4)	1.157(4)			1.150(4)	1.150(7)

Table S1 Cont'd.

	5·TCNQ$_2$ **A**	**5**·TCNQ$_2$ **B**
C1-C2	1.421(7)	1.431(7)
C2-C3	1.388(6)	1.392(5)
C2-C9	1.422(6)	1.413(6)

C3-C4	1.439(5)	1.442(5)
C3-C10	1.433(7)	1.433(6)
C4-C5	1.361(6)	1.348(5)
C5-C6	1.436(7)	1.425(7)
C6-C7	1.404(6)	1.402(6)
C6-C11	1.430(5)	1.435(5)
C7-C8	1.413(6)	1.425(7)
C7-C12	1.426(7)	1.424(8)
C10-C11	1.357(6)	1.350(5)

Table S2 Charge of TCNQ radicals, estimated by geometric correlations proposed by Kistenmacher *et al*. [28]. Bond lengths in **1**·I·TCNQ are not accurate enough and did not yield reasonable estimates of charge.

	ring A	ring B	ring C	ring D	ring E
1$_2$·TCNQ$_5$·MeCN	−1.08	−0.68	−0.11	−1.00	−0.89
2·TCNQ$_2$·MeCN	−0.88				
3$_2$·TCNQ$_3$	−0.51	−0.85	−0.85	−0.19	
4·TCNQ$_3$	−0.50	−0.75			
5·TCNQ$_2$	−0.55	−0.50			

S3 EPR results

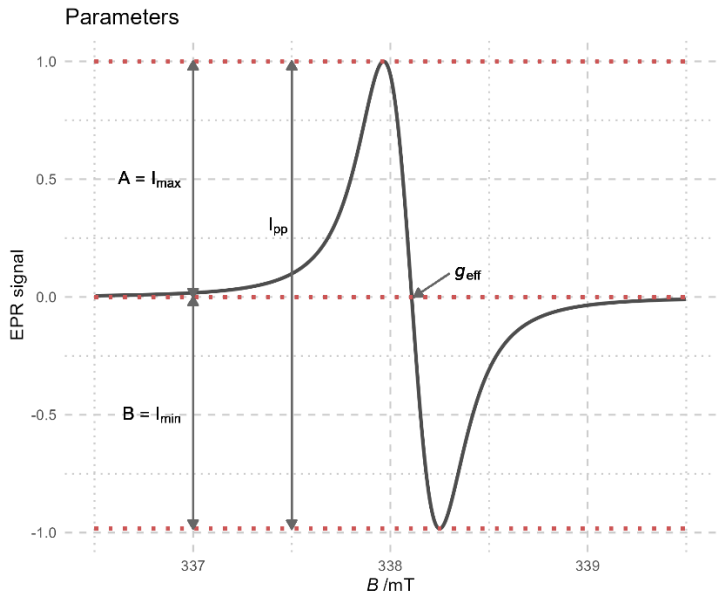

Figure S13 Standard EPR spectra and definition of values *A*, *B*, I_{pp} and g_{eff}.

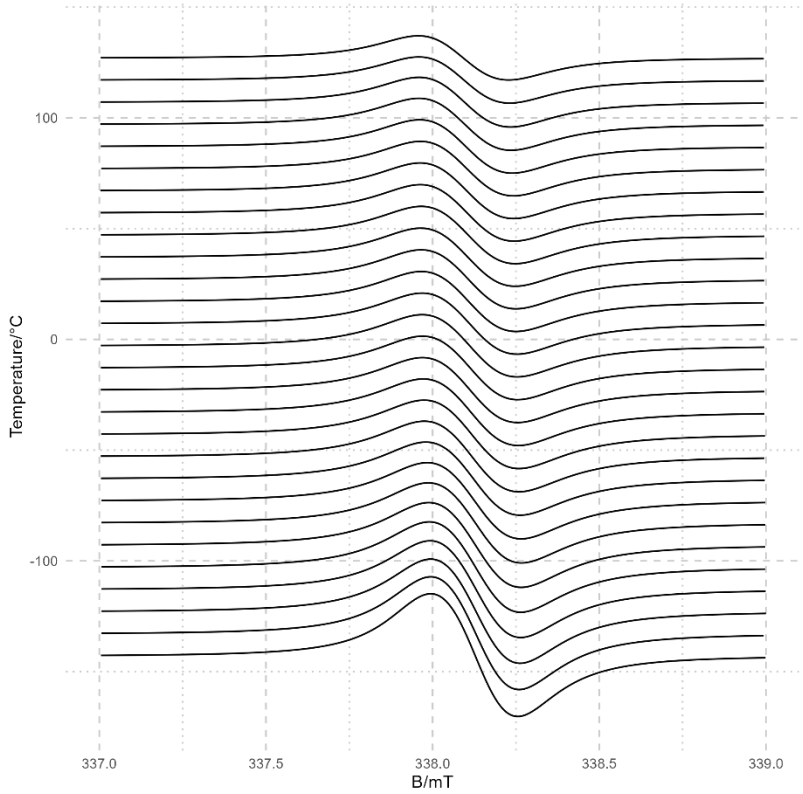

Figure S14 X-band EPR spectra (in arbitrary units) of **1**·I·TCNQ recorded at different temperatures between 120 and 400 K.

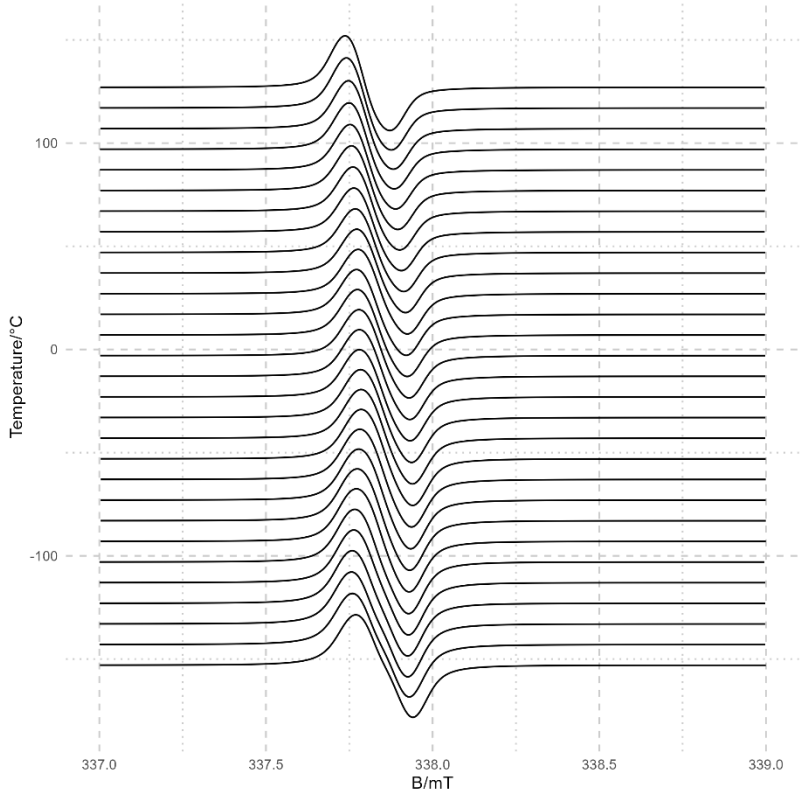

Figure S15 X-band EPR spectra (in arbitrary units) of $\mathbf{1}_2$·$TCNQ_5$·MeCN recorded at different temperatures between 120 and 400 K.

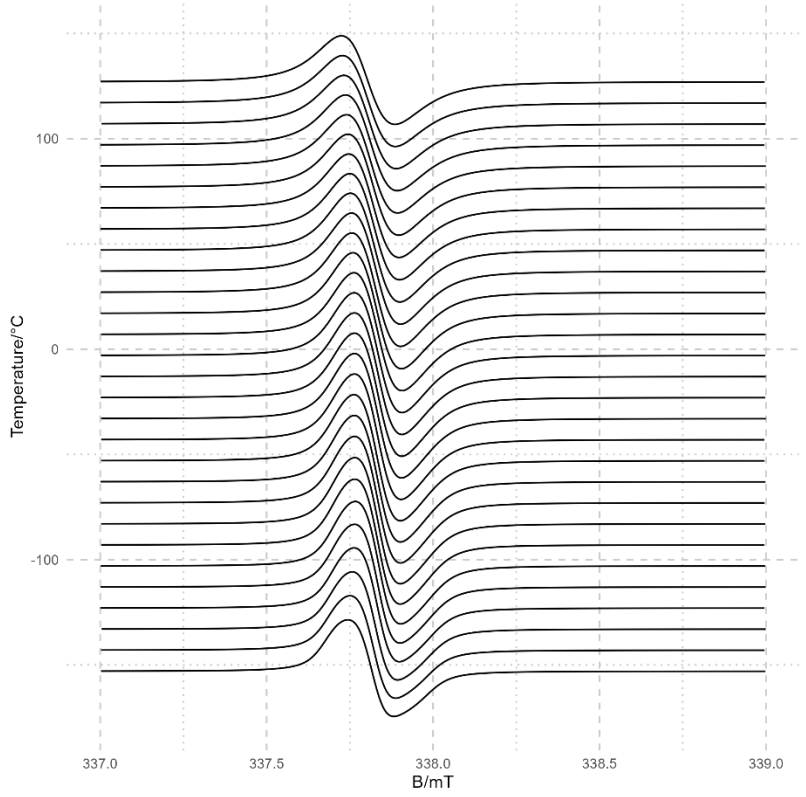

Figure S16 X-band EPR spectra (in arbitrary units) of **2**·$TCNQ_2$·MeCN recorded at different temperatures between 120 and 400 K.

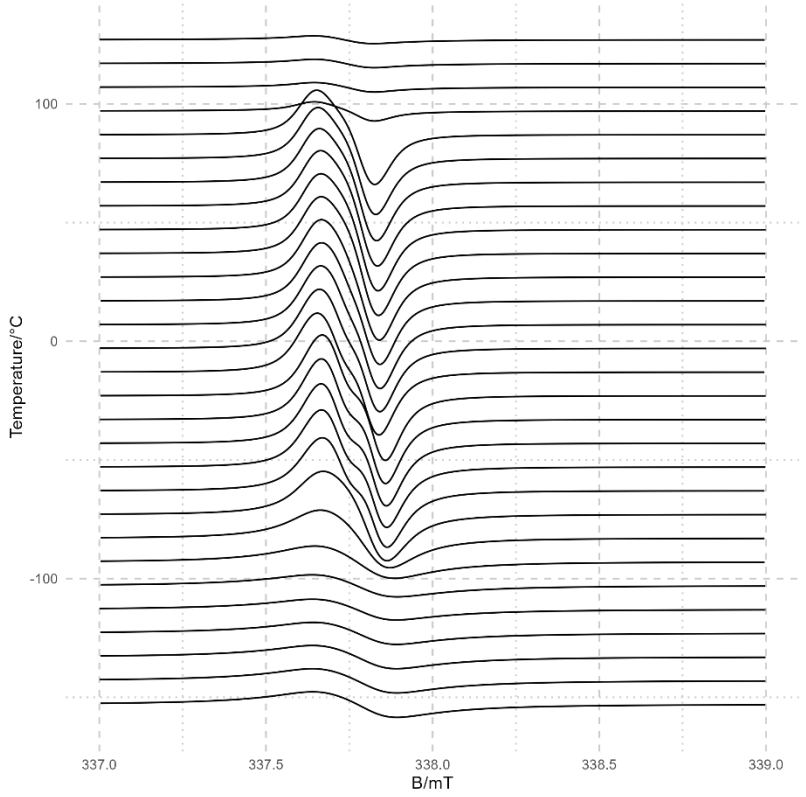

Figure S17 X-band EPR spectra (in arbitrary units) of $\mathbf{3}_2$·$TCNQ_3$ recorded at different temperatures between 120 and 400 K.

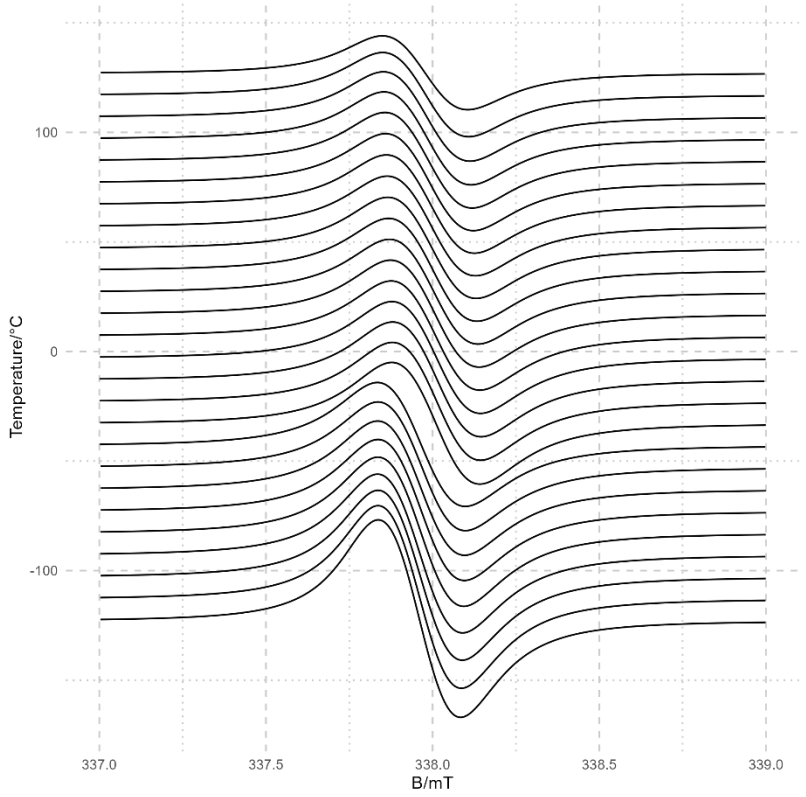

Figure S18 X-band EPR spectra (in arbitrary units) of **5**·$TCNQ_2$ recorded at different temperatures between 120 and 400 K.

a) b)

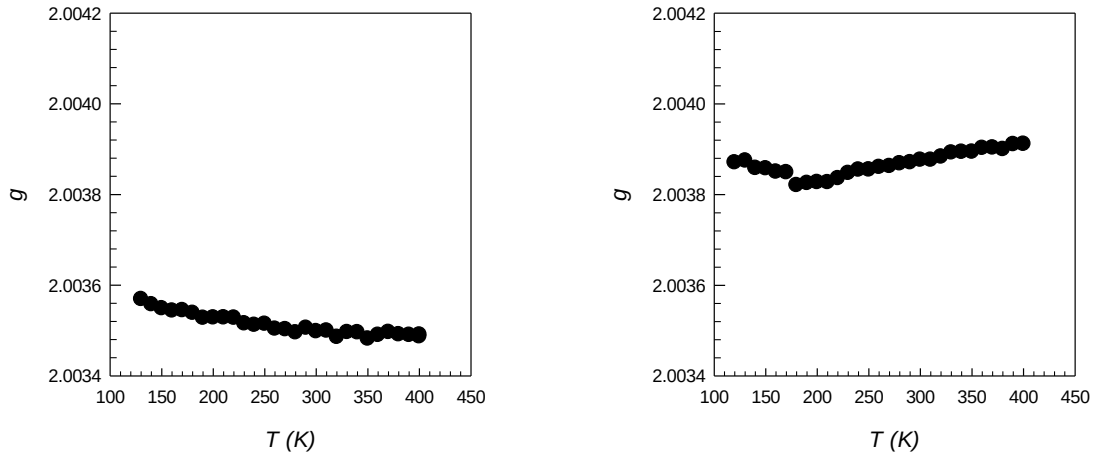

c) d)

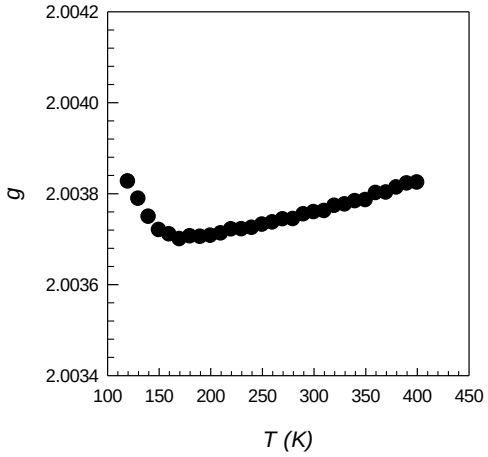

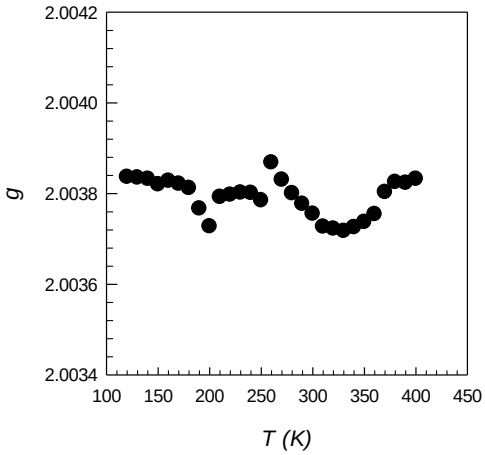

e)

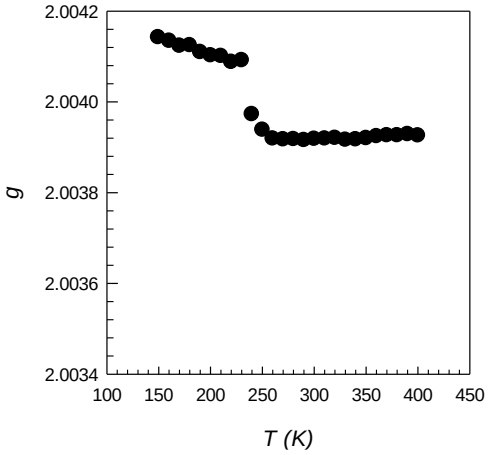

Figure S19 Temperature dependence of g_{eff} values for samples a) **1**·I·TCNQ, b) **1**$_2$·TCNQ$_5$·MeCN, c) **2**·TCNQ$_2$·MeCN, d) **3**$_2$·TCNQ$_3$ and e) **5**·TCNQ$_2$.

a) b)

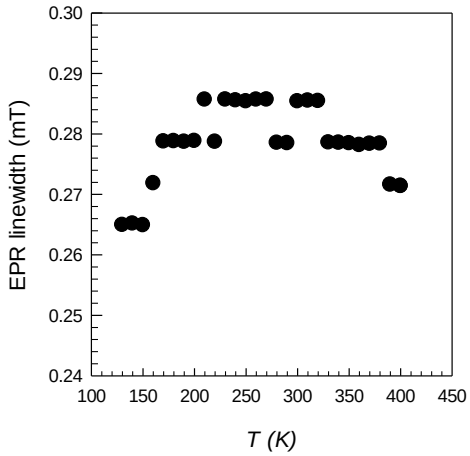
EPR linewidth (mT)
T (K)

c)

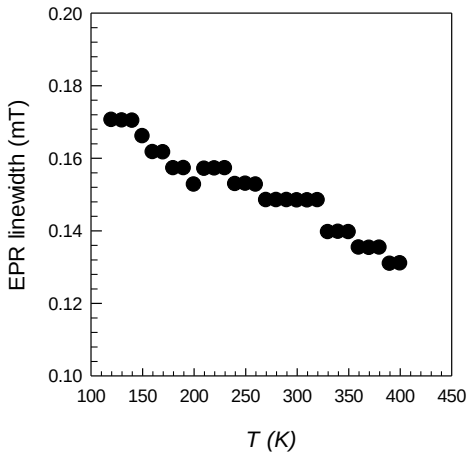
EPR linewidth (mT)
T (K)

d)

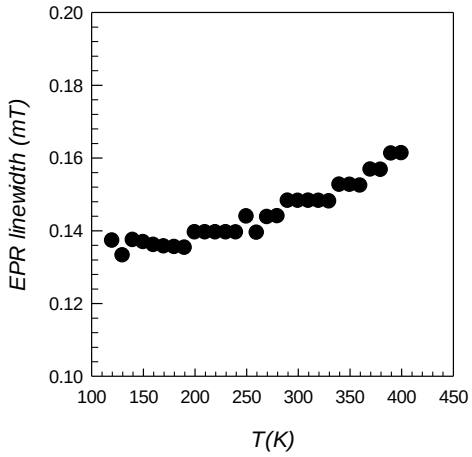
EPR linewidth (mT)
T(K)

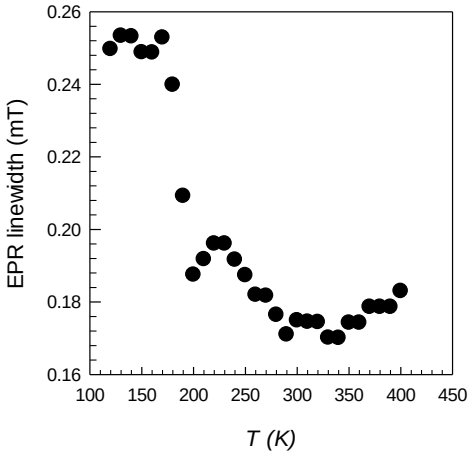
EPR linewidth (mT)
T (K)

e)

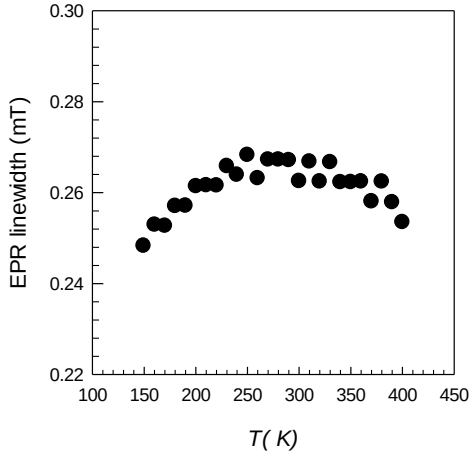

Figure S20 Temperature dependence of ERP linewidth for samples a) **1**·I·TCNQ, b) **1**$_2$·TCNQ$_5$·MeCN, c) **2**·TCNQ$_2$·MeCN, d) **3**$_2$·TCNQ$_3$ and e) **5**·TCNQ$_2$.

a) b)

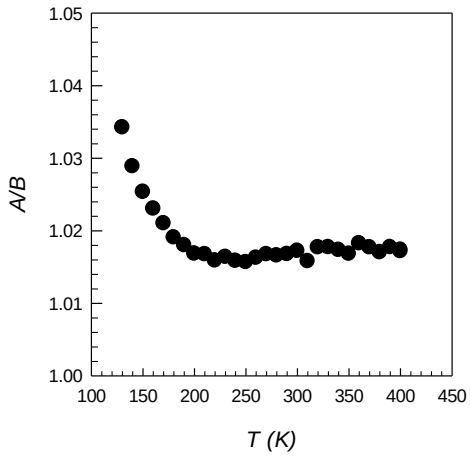
1.05
1.04
1.03
1.02
1.01
1.00
A/B
100 150 200 250 300 350 400 450
T (K)

c)

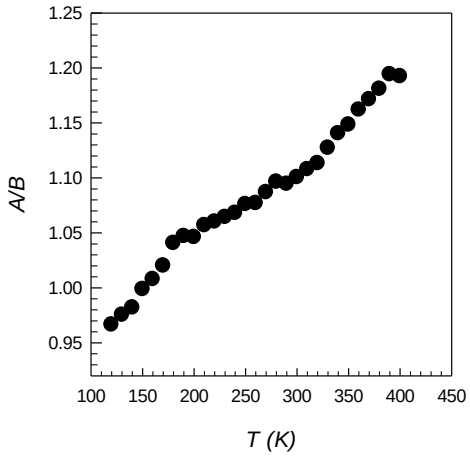
1.25
1.20
1.15
1.10
1.05
1.00
0.95
A/B
100 150 200 250 300 350 400 450
T (K)

d)

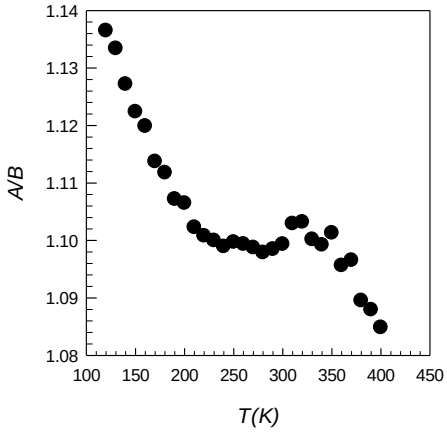
1.14
1.13
1.12
1.11
1.10
1.09
1.08
A/B
100 150 200 250 300 350 400 450
T(K)

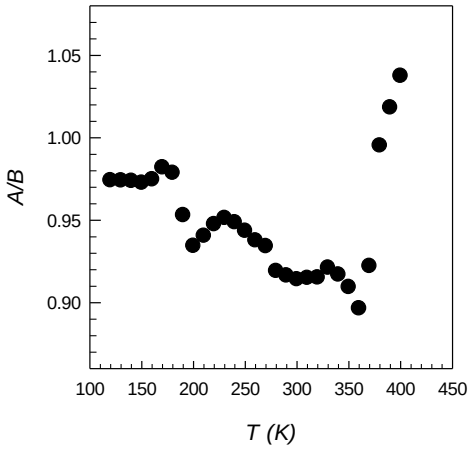
1.05
1.00
0.95
0.90
A/B
100 150 200 250 300 350 400 450
T (K)

e)

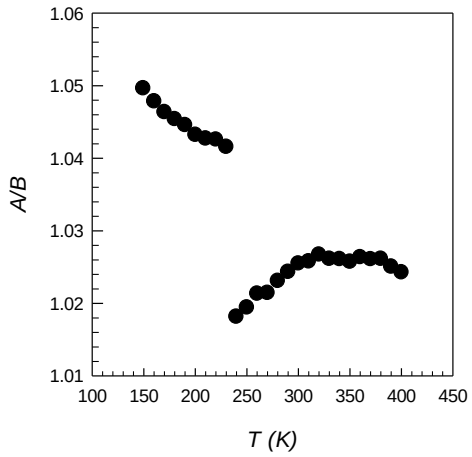

Figure S21 Temperature dependence of A/B ratio as a measure of the asymmetry of the EPR lines for samples a) **1**·I·TCNQ, b) **1**$_2$·TCNQ$_5$·MeCN, c) **2**·TCNQ$_2$·MeCN, d) **3**$_2$·TCNQ$_3$ and e) **5**·TCNQ$_2$.

S4 Magnetization measurements

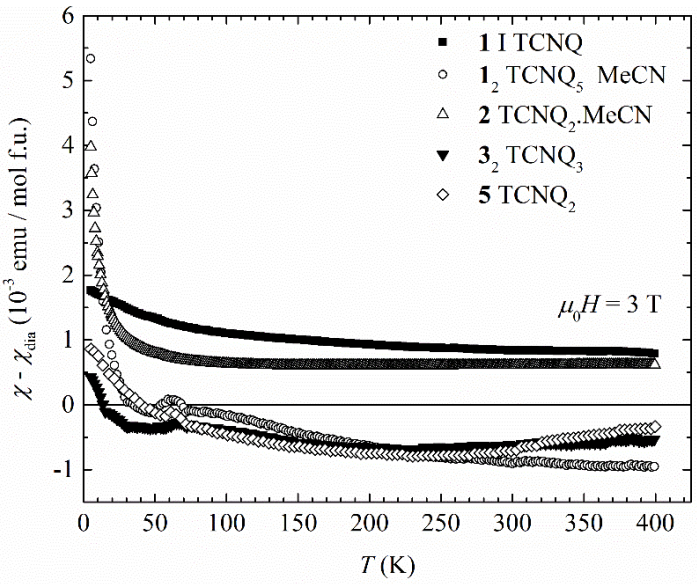

Figure S22 Temperature dependence of magnetic susceptibility with subtracted diamagnetic contributions (see table S3).

Table S3 Calculated diamagnetic contribution to susceptibilities in emu/mol f.u. using tables from ref. [33]. These contributions are subtracted from the total susceptibility of the sample (shown in Fig. 10 in the main text), and the resulting susceptibility $\chi - \chi_{dia}$ is shown in Fig. S22.

1·I·TCNQ	**1**$_2$·TCNQ$_5$·MeCN	**2**·TCNQ$_2$·MeCN	**3**$_2$·TCNQ$_3$	**5**·TCNQ$_2$
$-2.0866 \cdot 10^{-4}$	$-6.6084 \cdot 10^{-4}$	$-3.2238 \cdot 10^{-4}$	$-4.9592 \cdot 10^{-4}$	$-3.2072 \cdot 10^{-4}$

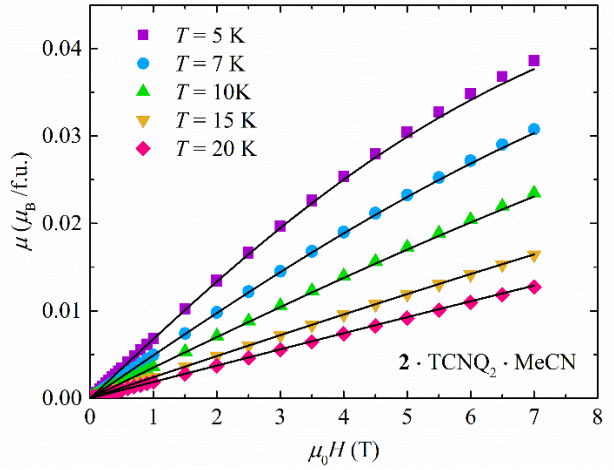

Figure S23 Dependence of the measured magnetic moment on magnetic field for 2·TCNQ$_2$·MeCN measured at different temperatures (symbols) compared to magnetization calculated using Eq. (SI 1) (lines).

The magnetization data plotted in Fig S23 are compared to

$$M(H, T) = c_i N_A g \mu_B S B_j(g, S, H, T) + (1-c_i) \chi_{1D\,HAF}(T) \cdot H + \chi_0 \cdot H \qquad \text{(SI 1)}$$

where the first term containing the Brillouin function $B_j(g, S, H, T)$ represents the contribution of impurities and the second term is the contribution of the $S = 1/2$ chain. Third term represents the temperature-independent contribution. N_A is Avogadro's constant, g is the electron g factor obtained from EPR, μ_B is Bohr magneton, S is spin, H is the applied magnetic field. The values of c_i and J are taken from the results of the fit of the susceptibility to Eq. 1 in the main text. We see that the same model describes the measured M vs. H curves very well.

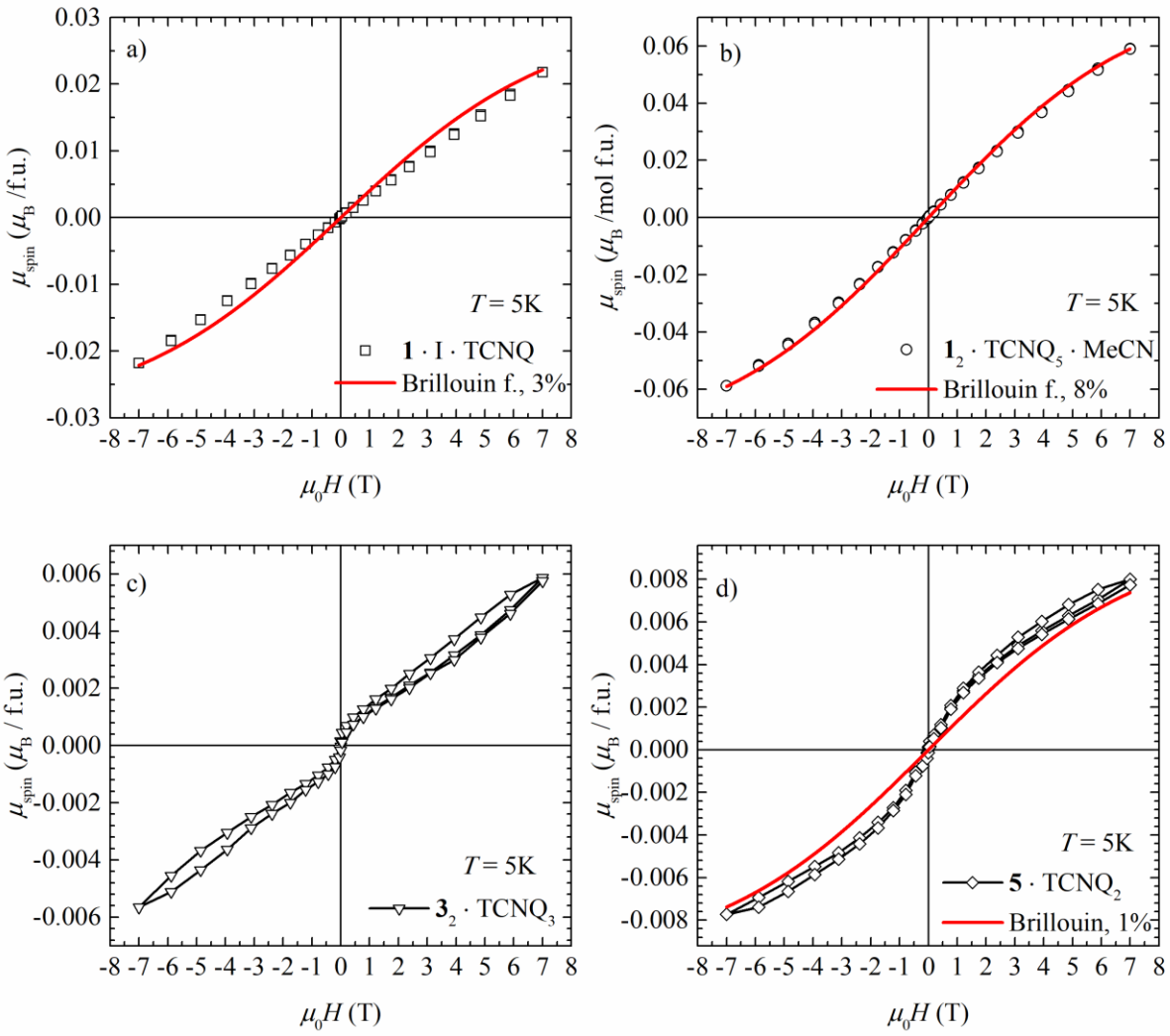

Figure S24 Dependence of magnetic moment on magnetic field measured at T = 5 K for a) **1**·I·TCNQ, b) $\mathbf{1}_2$·TCNQ$_5$·MeCN, c) $\mathbf{3}_2$·TCNQ$_3$ and d) **5**·TCNQ$_2$. The solid red line represents the S = 1/2 Brillouin function for several percent of unpaired spins. The hysteresis observed for $\mathbf{3}_2$·TCNQ$_3$ and **5**·TCNQ$_2$ suggests a weak ferromagnetic state might be the ground state of these two systems.